3D structural human interactome reveals proteome-wide perturbations by disease mutations

Dapeng Xiong[1,2,3,11], Junfei Zhao[4,11], Yunguang Qiu[5,11], Yadi Zhou[5,11], Dongjin Lee[1,2,11], Shobhita Gupta[2,3,6,11], Weiqiang Lu[7], Siqi Liang[1,2], Jin Joo Kang[1,2,3], Charis Eng[5,8,9], Joseph Loscalzo[10], Feixiong Cheng[5,8,9,*], Haiyuan Yu[1,2,3,12,*]

[1]Department of Computational Biology, Cornell University, Ithaca, NY 14853, USA

[2]Weill Institute for Cell and Molecular Biology, Cornell University, Ithaca, NY 14853, USA

[3]Center for Innovative Proteomics, Cornell University, Ithaca, NY 14853, USA

[4]Department of Systems Biology, Herbert Irving Comprehensive Center, Columbia University, New York, NY 10032, USA

[5]Genomic Medicine Institute, Lerner Research Institute, Cleveland Clinic, Cleveland, OH 44195, USA

[6]Biophysics Program, Cornell University, Ithaca, NY 14853, USA

[7]Shanghai Key Laboratory of Regulatory Biology, Institute of Biomedical Sciences and School of Life Sciences, East China Normal University, Shanghai 200241, China

[8]Department of Molecular Medicine, Cleveland Clinic Lerner College of Medicine, Case Western Reserve University, Cleveland, OH 44195, USA

[9]Case Comprehensive Cancer Center, Case Western Reserve University School of Medicine, Cleveland, OH 44106, USA

[10]Channing Division of Network Medicine, Division of Cardiovascular Medicine, Department of Medicine, Brigham and Women's Hospital, Harvard Medical School, Boston, MA 02115, USA

[11]These authors contributed equally

[12]Lead contact

*Correspondence: chengf@ccf.org (F.C.), haiyuan.yu@cornell.edu (H.Y.)

SUMMARY

Human genome sequencing studies have identified numerous loci associated with complex diseases. However, translating human genetic and genomic findings to disease pathobiology and therapeutic discovery remains a major challenge at multiscale interactome network levels. Here, we present a deep-learning-based ensemble framework, termed PIONEER (**P**rotein-protein **I**nteracti**O**n i**N**t**E**rfac**E** p**R**ediction), that accurately predicts protein binding partner-specific interfaces for all protein interactions in humans and seven other common model organisms. We demonstrate that PIONEER outperforms existing state-of-the-art methods. We further systematically validated PIONEER predictions experimentally through generating 2,395 mutations and testing their impact on 6,754 mutation-interaction pairs, confirming PIONEER-predicted interfaces are comparable in accuracy as experimentally determined interfaces using PDB co-complex structures. We show that disease-associated mutations are enriched in PIONEER-predicted protein-protein interfaces after mapping mutations from ~60,000 germline exomes and ~36,000 somatic genomes. We identify 586 significant protein-protein interactions (PPIs) enriched with PIONEER-predicted interface somatic mutations (termed oncoPPIs) from pan-cancer analysis of ~11,000 tumor whole-exomes across 33 cancer types. We show that PIONEER-predicted oncoPPIs are significantly associated with patient survival and drug responses from both cancer cell lines and patient-derived xenograft mouse models. We identify a landscape of PPI-perturbing tumor alleles upon ubiquitination by E3 ligases, and we experimentally validate the tumorigenic KEAP1-NRF2 interface mutation p.Thr80Lys in non-small cell lung cancer. We show that PIONEER-predicted PPI-perturbing alleles alter protein abundance and correlates with drug responses and patient survival in colon and uterine cancers as demonstrated by proteogenomic data from the National Cancer Institute's Clinical Proteomic Tumor Analysis Consortium. PIONEER, implemented as both a web server platform and a

software package, identifies functional consequences of disease-associated alleles and offers a deep learning tool for precision medicine at multiscale interactome network levels.

KEYWORDS

Protein-protein interaction (PPI) interfaces, deep learning, 3D structural interactomes, disease-associated mutations, oncoPPIs, proteome-wide perturbations, pharmacogenomic landscape, proteogenomic perturbation

INTRODUCTION

Precision medicine has sparked major initiatives focusing on whole-genome/exome sequencing (WGS/WES) and developing genome science tools for statistical analyses – all aspiring to identify actionable variants in patients (Braberg et al., 2022; Cheng et al., 2019; Nussinov et al., 2022). At the center of the massive amount of collected DNA/RNA sequencing data is their functional interpretation, which largely rests on conventional statistical analyses and trait/phenotype observations (Braberg et al., 2022). Statistics is vital, since it guides the identification of disease-associated variants; however, traditional WGS/WES studies are commonly underpowered for disease risk-variant/gene and drug target discoveries as very large sample sizes are generally required. Furthermore, the statistics does not directly elucidate the functional consequence of the variants, i.e., changes in protein conformation or in molecular functions in cells; thus, it may not be sufficient to define accurately functional variants. Thus, translation of genetic and genomic findings to precision medicine is fraught with challenges using traditional statistical approaches.

Optimal information requires knowledge of the whole protein-protein interaction (PPI) network, or interactome, within which the mutant protein operates. Given that on average each protein interacts directly with 10-15 other proteins (Barabási et al., 2011; Vidal et al., 2011), the functional consequence of any mutation is not easily (if at all) predicted out of the interactome context. Previous studies (Cheng et al., 2019; Cheng et al., 2021; Meyer et al., 2018; Sahni et al., 2015; Wang et al., 2012; Wierbowski et al., 2021) have demonstrated that most disease mutations disrupt specific protein-protein interactions rather than affecting all of protein-protein interactions in which the mutant

protein is engaged; and making accurate dissection of such disruptions is essential for understanding the etiology of most disease mutations. Therefore, it is fundamentally important for precision medicine to determine structural details, particularly the locations of interaction interfaces of all protein interactions at whole proteome scale. A clear limitation of this goal, however, is that only ~9% of protein interactions have structural models determined by experimental or traditional homology modeling approaches (Figure 1A and 2A).

In this study, we presented a deep-learning-based ensemble learning pipeline, PIONEER (**P**rotein-protein **I**nteracti**O**n i**N**t**E**rfac**E** p**R**ediction) to generate the next-generation partner-specific three-dimensional (3D) human interactome with significant improvement in both quality and coverage, and we validated many of our findings experimentally. By leveraging the available atomic-resolution co-crystal structures along with homology models, we established a comprehensive multiscale 3D structural interactome, which consists of 282,095 interactions from humans and seven other commonly studied organisms, and includes all 146,138 experimentally determined PPIs for 16,232 human proteins (Figures 1A and 2A). Through this resource, we investigated the network effects of disease-associated mutations at amino acid resolution within the 3D macromolecular interactome of PPI interfaces. We further explored the widespread perturbations of PPIs in human diseases and their significant impact on disease prognosis and drug responses. This newly constructed 3D interactome database is then combined with disease-associated mutations and functional annotations to create an interactive, dynamic web server (https://pioneer.yulab.org) for genome-wide functional genomics studies. It also allows the users to submit a list of interactions and retrieve the predicted

interfaces of the respective interactions using the PIONEER framework. Furthermore, we have converted the PIONEER framework into a software package that is available to the wider community to further help accelerate biological research.

RESULTS

A hybrid deep-learning architecture for protein-protein interface prediction

To date, taking into account the structural models of protein interactions--both experimentally determined and homologically predicted--we find that an overwhelming majority of interactions (~91%) still do not have reliable structural information (Figure 1A). With this key limitation in mind, we built the PIONEER pipeline to generate accurate partner-specific protein-protein interface predictions for protein interactions that currently lack structural information. We carefully constructed our labeled dataset for training, validating, and testing of our classifiers (Dataset S1). Compared to our previous ECLAIR dataset (Meyer et al., 2018), PIONEER's dataset is much larger since many parameters need to be tuned by the deep learning classifier to allow for a more accurate and powerful model. It is worth noting that the ECLAIR training set was not designed to prioritize specifically cases where the same protein interacts with multiple interaction partners using distinct interfaces; thus, when building PIONEER, we especially prioritize such instances in our labeled dataset in order to create a model that better predicts partner-specific interfaces (Figure 1B). In particular, we require that there are no homologous interactions between any of the two datasets to guarantee the robustness and generalization of our models, and a fair performance evaluation. To this end, we generate 2,615 (>6 times larger than the previous ECLAIR training set), 400, and 400 interactions

for the new training, validation, and testing sets from the PDB (Burley et al., 2022), respectively.

We used a comprehensive set of single-protein and interaction-partner-specific features for interface prediction (Figures 1C-1F), and both groups of features combine biophysical, evolutionary, structural, and sequence information for an in-depth feature characterization. More specifically, the single-protein features consist of diverse biophysical features, evolutionary sequence conservation, and protein structure properties. Of these features, one of protein structure properties, solvent accessible surface area (SASA), is widely reported to be highly informative (Meyer et al., 2018; Xue et al., 2015) since all interface residues, by definition, are on the surface of proteins; in addition, solvent can either facilitate or impede binding interactions depending upon the (net) relative hydrophobicity or hydrophilicity of the binding interaction residues. We also incorporate evolutionary sequence conservation because key protein functions often depend upon interactions with other proteins, and, as such, interface residues are more likely to be conserved (Guharoy and Chakrabarti, 2010).

However, although these single-protein features capture the characteristics of all possible interface residues, they cannot distinguish interface residues for a protein interacting with different partner proteins through which a protein can perform different functions biologically. Previously, we illustrated that it is important to encompass partner-specific features for the prediction of partner-specific interfaces (Meyer et al., 2018). Here, our interaction-partner-specific features include co-evolution of amino acid sequences, protein-protein docking, and pair potential. Co-evolutionary features capture the dependent patterns of conservation in two interacting proteins, since interface residues

that are critical to maintaining the interaction often co-evolve so as to maintain binding complementarity (Mintseris and Weng, 2005). Through modeling of bound conformations of protein interactions using protein-protein docking (Pierce et al., 2014), we incorporate the docking results to extract a summary of preferred orientations for individual structures of interacting proteins. In addition, we also create another feature--pair potential--to characterize specifically the interface propensity for the target protein with respect to a specific partner. Moreover, we incorporate AlphaFold2-predicted single protein structures into our PIONEER models to significantly increase the coverage of structure-based features for proteins currently lacking experimentally determined structures.

In order to address the non-random missing feature problem, which cannot be adequately resolved by commonly used imputation methods (Meyer et al., 2018), PIONEER's framework is structured as an ensemble of four deep learning architectures, including Structure-Structure, Structure-Sequence, Sequence-Structure, and Sequence-Sequence models (Figures 1C-1F and S1-S2). The Structure-Structure model is used for interactions in which both proteins have structure information while the Sequence-Sequence model is used for proteins without solved structure information. Otherwise, the Structure-Sequence or Sequence-Structure model is used, depending on which protein in the interaction has structure information. This comprehensive framework ensures that we use the maximum amount of information available for each interaction to yield the best possible interface predictions while avoiding potential ascertainment biases that can lead to overfitting.

More specifically, for a protein with available structures, the PIONEER deep learning model uses a hybrid architecture to integrate both structure information

embedded through Graph Convolutional Networks (GCNs) with Auto-Regressive Moving Average (ARMA) filters (Bianchi et al., 2022) and sequence information embedded through bidirectional Recurrent Neural Networks (RNNs) with Gated Recurrent Units (GRUs) (Cho et al., 2014). For proteins without high-quality structure models, only sequence information is embedded via RNNs with GRUs. Using transfer learning (Zhuang et al., 2021), the pre-trained GCNs-RNNs in Structure-Structure model and RNNs in Sequence-Sequence model are deployed in Structure-Sequence model and Sequence-Structure model for the processing of proteins with and without structure information, respectively. Furthermore, for each residue in a target protein, our unique architecture integrates the residue embeddings, overall protein embeddings, and overall partner protein embeddings to utilize both local and global ('glocal') information of both proteins to make the most accurate interface predictions.

Benchmark evaluation of PIONEER

We then built and evaluated PIONEER using the new labeled dataset and new model designs. The results show that PIONEER outperforms all other available methods for predicting interactions of both proteins with and without structure information through a wide range of measures, including area under the receiver-operating characteristic curve (AUROC) and area under the precision-recall curve (AUPR) (Figures 2B-2E and S3-S4; Tables S1-S5). It is worth noting that our Sequence-Sequence model, which solely relies on sequence information, has better prediction performance than all recent state-of-the-art structure-based methods that we evaluated, such as ScanNet (Tubiana et al., 2022), BIPSPI+ (Sanchez-Garcia et al., 2022), DeepPPISP (Zeng et al., 2020), SASNet

(Townshend et al., 2019), and PIPGCN (Fout et al., 2017). Most of these methods already use cutting-edge deep learning models, which illustrates the power of utilizing a comprehensive set of single-protein and partner-specific features; it also confirms the validity of our design choice to include RNNs with GRUs in a hybrid architecture, even for proteins with known structures (Figures 2B-2C; Tables S2-S3). Interestingly, we also found that even our previous ECLAIR with structure information is still significantly better than the above structure-based methods, and achieves the second best performance (Figures 2B-2C; Table S2).

We next evaluated the effectiveness of our new model designs on the benchmark testing dataset by assessing the overall performance of PIONEER and ECLAIR. We found that PIONEER models with ECLAIR features substantially outperform our previous ECLAIR models (Figures S5A-S5B), confirming that our unique hybrid-architecture deep learning models, indeed, capture more information in the features than the previous random forest-based models. Moreover, incorporating new features to PIONEER models further significantly improves the prediction performance (Figures S5A-S5B), indicating the outstanding representation ability of our new features for the prediction of protein interfaces. Both improvements distinctly demonstrate that our new deep learning architectures and new features make significant contributions to PIONEER's strong ability to provide accurate PPI interface predictions. We also found that the inclusion of AlphaFold2-predicted single protein structures for the proteins without experimentally determined structures improved the performance of PIONEER interface predictions (Figures S5C-S5D).

Proteome-wide protein-protein interface prediction by PIONEER

Next, we compiled a comprehensive set of experimentally validated binary PPIs for humans and seven model organisms by integrating information from 7 commonly-used databases (Das and Yu, 2012), including BioGRID (Oughtred et al., 2019), DIP (Salwinski et al., 2004), IntAct (Orchard et al., 2014), MINT (Licata et al., 2012), iRefWeb (Turner et al., 2010), HPRD (Keshava Prasad et al., 2009), and MIPS (Mewes et al., 2011). Here we focus on binary interactions because if two proteins do not bind to each other directly, the concept of interface does not apply. We then used the fully-optimized PIONEER pipeline to predict interfaces for all collected 256,946 binary interactions without any experimental structures or homologous models, including 132,875 human interactions (Figure 2A). Because we make partner-specific interface predictions for every residue of every protein, and there are on average >10 interactions per protein, we made probabilistic interaction predictions for >275 million residue-interaction pairs. By combining our PIONEER interface predictions with 25,149 interactions (~9%) with experimental or homology models, we generate a comprehensive multiscale 3D human interactome, in which all interactions have partner-specific interface information at the residue level, together with atomic-resolution 3D models whenever possible.

To comprehensively evaluate the quality of our predicted interfaces and their biological implications, we first carried out large-scale mutagenesis experiments to measure the fraction of disrupted interactions by mutations in our predicted interfaces at varying confidence levels, in comparison to that of known interface and non-interface residues from co-crystal structures in the PDB. Using our Clone-seq pipeline (Wei et al., 2014), we generated 2,395 mutations on 1,141 proteins and examined their impact on

6,754 mutation-interaction pairs through a high-throughput yeast-two-hybrid (Y2H) assay, an unprecedented large-scale experimental validation. We observed that mutations at PIONEER-predicted interfaces disrupt protein-protein interactions at a very similar rate to the mutations at known structurally characterized interfaces, and both of their disruption rates are significantly higher than that of known non-interfaces (Figure 2F). Therefore, our large-scale experiments confirm the high quality of our interface predictions and the validity of our overall PIONEER pipeline. Furthermore, because interaction disruption is key to understanding the molecular mechanisms of disease mutations (Sahni et al., 2015; Wei et al., 2014), our experimental results indicate that our PIONEER-predicted interfaces will be instrumental in prioritizing disease-associated variants and generating concrete mechanistic hypotheses.

PIONEER-generated 3D human interactome enriched with disease mutations

Since disruption of specific interactions is essential for the pathogenicity of many disease mutations, and since previous studies have shown that disease mutations are significantly enriched at protein-protein interfaces (Cheng et al., 2021; Wang et al., 2012; Xiong et al., 2022), we next measured the enrichment of known disease-associated mutations from the Human Gene Mutation Database (HGMD) (Stenson et al., 2017) at the predicted interfaces, and compared it to known interfaces from co-crystal structures. We found that the residues predicted by PIONEER with a high interface confidence show a very similar rate of disease mutation enrichment to those of known interfaces (Figure 3A). Furthermore, we observed that up to ~98% of all 256,946 binary interactions have at least one or more predicted interface residues that fall into high or very high confidence

categories (Figure S6), indicating that PIONEER provides meaningful structural information for the vast majority of protein interactions. In fact, each bin with a higher confidence of predicted interfaces is more likely to contain disease-associated mutations than the previous bin, which demonstrates the strong correlation between PIONEER prediction scores and the true function of each residue (Figure 3A). We further analyzed the distribution of population genetic variants and found that their enrichment in PIONEER-predicted interfaces and non-interfaces also matches well with that of known interfaces and non-interfaces, respectively (Figure 3B). The results also show that there is a depletion of common variants (i.e., not deleterious) in both known and predicted interfaces, which strongly suggests that there exists a strong negative selection at these interface residues, indicating that PIONEER is able to predict functionally important interface variants effectively. We also found that, compared to variants identified in individuals from the 1000 Genomes project (1KGP) (Auton et al., 2015) and the Exome Aggregation Consortium (ExAC) (Lek et al., 2016), disease-associated mutations from HGMD are more significantly enriched at PPI interfaces of the respective proteins (Cheng et al., 2021) (Figure 3C). Moreover, as predicted by CADD (Kircher et al., 2014) and FoldX (Schymkowitz et al., 2005), the population variants in PIONEER-predicted interfaces are more likely to adversely affect protein functions than those in PIONEER-predicted non-interfaces (Figure S7), which confirms that deleterious variants preferentially occur at the protein-protein interfaces (Sahni et al., 2015; Wang et al., 2012).

To further evaluate whether the disease-associated mutations were enriched in the PIONEER-predicted PPI interfaces (Figure 3C), we next categorized the disease-associated germline mutations from HGMD into six major disease groups, including

autoimmune, cancer, cardiovascular, metabolic, neurological, and pulmonary as described in a recent study (Zhou et al., 2020), as well as an additional “other” category. We identified a total of 10,753 PPIs among 5,684 proteins that had at least one disease-associated interface germline mutation (Figure 3D; Table S6), among which 9,795 (~91%) PPIs have such interface mutations on one protein (the other protein colored as “neighbor”), and 958 (~9%) on both proteins of the binding pair. Overall, this network analysis shows that PIONEER-predicted PPI interfaces are altered by broad disease-associated mutations across multiple disease categories. To highlight the usefulness of PIONEER-predicted interfaces, we examined three PPI interfaces with germline alleles. Germline mutation p.Lys542Gln of LMNA (Lamin A/C) buried in the interface of LMNA and BAF (Figure 3E) was associated with progeroid disease (Plasilova et al., 2004). One loss-of-function PPIA mutation p.Ala53Glu in the interface of PPIA-SYUA (Figure 3E) was identified in patients with early-onset Parkinson disease (Favretto et al., 2020). A germline mutation p.Gly537Arg of HIF-2α associated with polycythemia vera (Liu et al., 2017) is located in the PIONEER-predicted VHL-HIF-2α interface (Figure 3E) and disrupts VHL binding via impairing ubiquitination and proteasomal degradation of HIF-2α (Tarade et al., 2018; V et al., 2012). Taken together, PIONEER-predicted protein-protein interface mutations convey crucial structural information in delineating the functional consequences for disease mechanisms at the atomic and allele levels.

PIONEER-predicted oncoPPIs across 33 cancer types

We next investigated the somatic mutations from cancer patients in the context of PPI interfaces inferred by PIONEER. In total, we collected ~1.7 million missense somatic

mutations from the analysis of ~11,000 tumors across 33 cancer types from The Cancer Genome Atlas (TCGA) (Chang et al., 2013). We found significant enrichment of somatic missense mutations in the PIONEER-predicted PPI interfaces compared to non-interface regions (Figure 4A, Dataset S2). Specifically, this significant enrichment was observed in 31 out of the total 33 cancer types regardless of the overall mutation burden. In lung squamous cell carcinoma (LUSC), one of the cancer types that have the highest mutation load per exome, we observed 29 variants per 1 million amino acid residues affecting PPI interfaces, while the rate for the non-PPI interface region is 23 ($P = 1.3\times10^{-11}$). For thyroid cancer (THCA), with the lowest mutation load, the difference is 27 for PPI interfaces vs. 9 for the remainder of the protein sequences ($P < 10^{-16}$). To account for the potential bias in this analysis due to data sources, we divided our whole 3D human interactome into three categories: those with experimental structures (PDB, 6.2%), with homology models (HM, 2.8%), and predicted by PIONEER (90.9%), and performed the enrichment analysis for each category separately. The results showed that the same enrichment pattern we observed is independent of the data source, suggesting the robustness of PIONEER interface predictions (Figure S8).

We next sought to identify the oncoPPIs that were significantly enriched by somatic mutations in the interfaces in both individual cancer types and pan-cancer analyses. Specifically, the average number of PPIs affected by interface mutations is 10,741. Finally, our analysis yielded total 586 statistically significant oncoPPIs across 33 cancer types (Figure 4B, Dataset S3), including KRAS-BRAF, TP53-EGLN1, and TP53-TP53BP2 across 10 cancer types.

We next turned to analyze the clinical sequencing data from MSK-MET, a pan-cancer cohort of over 25,000 patients spanning 50 different tumor types (Nguyen et al., 2022). Of the 157,979 missense mutations we investigated, 40,526 (~26%) were identified to affect 15,523 unique PPI interfaces. Focusing on the PPIs that were disturbed in at least 10 samples in a specific cancer type, we performed survival analysis to identify clinically actionable oncoPPIs whose disruption is significantly associated with patient survival. KRAS has been reported to co-mutate with NF1 (neurofibromin protein) in response to GTP hydrolysis (Rabara et al., 2019). We identified that the mutations of KRAS-NF1 interface residues, such as Asp30 and Glu31 on KRAS (Figure 5A), are significantly associated with poor survival rate compared to the wild-type (WT) group in pancreatic cancer (P = 2.7×10^{-18}) (Figure 5B). SPOP plays a multifaceted role in oncogenesis and progression by mediating degradation of PTEN (Wang et al., 2020), BRD3 (Ostertag et al., 2019a) , TP53BP1 (Wang et al., 2021), PDX1 (Ostertag et al., 2019b), and MACROH2A1 (Hernández-Muñoz et al., 2005). The SPOP MATH domain binds to PTEN via a PIONEER-predicted interface mutation of p.Phe133Val on SPOP (Song et al., 2020), which is significantly associated with survival rate in prostate cancer (P = 0.0021) (Figure 5B). Patients with several PIONEER-predicted interface mutations (Thr231, Pro191 and Arg181 on TP53; Figure 5A) between TP53 (a key tumor suppressor gene) and KDM4D (a histone demethylase) are significantly associated with poor survival in soft tissue sarcoma (P = 0.031) (Figure 5B). OncoPPI analysis revealed that PIONEER-predicted interface mutations in ARIH2-TP53, kinase-substrate (e.g., KIT-BLK), kinase-E3 ligase (e.g., MAPKAPK3-FBXW7), and cyclin-E3 ligase (e.g., CCND1-FBXO31), are significantly associated with survival rate in breast cancer (P = 1×10^{-4}), gastrointestinal

stromal tumor (*P* = 0.011), non-small cell lung cancer (*P* = 0.012), and endometrial cancer (*P* = 0.024), respectively (Figures 5B and S9). Accumulated evidence suggested the mutations of CCND1 are associated with multiple cancer types (Xu and Lin, 2018). By analyzing PIONEER-predicted oncoPPIs, we found PIONEER-predicted interface mutations of CCND1 are significantly enriched at the CCND1-CDK4 interfaces in uterine cancer (*P* = 0.012) and low-grade glioma (*P* = 0.048). We identified that CCND1 not only interacts with CDK4 but also TSC2 from PIONEER-predicted interfaces. Specifically, we identified that CCND1 interacts with CDK4 and TSC2 via two unique sets of interfaces (Figure 5C). Next, we experimentally confirmed this result using co-immunoprecipitation with 293T cells. Figure 5D shows that a mutation of p.Lys114Arg on CCND1 specifically disrupts the interaction between CCND1 and CDK4, without disrupting its interaction with TSC2. Interestingly, mutation p.Glu162Lys on CCND1 does not disrupt its interaction with CDK4, but does disrupt its interaction with TSC2. Both p.Lys114Arg and p.Glu162Lys on CCND1 are associated with myeloma (Ryu et al., 2020) and lung cancer (Zhang et al., 2017), respectively. These results further demonstrate that PIONEER-generated 3D human interactome can uncover tumorigenesis with distinctive functions corresponding to distinct interfaces, even for those on the same proteins.

PIONEER-predicted PPI-perturbing tumor alleles alter ubiquitination by E3 ligases

E3 ubiquitin ligases (E3s) are involved in cellular transformation and tumorigenesis by targeted protein degradation (Mészáros et al., 2017; Yang et al., 2021). Identifying how somatic mutations alter PPIs of E3 ligases may offer novel targets for development of targeted protein degradation therapies (Senft et al., 2018). We investigated 4,614

PIONEER-predicted oncoPPIs connecting 355 E3 ligases annotated from E3net (Han et al., 2012) and Ubinet2.0 (Li et al., 2021b) databases. We next focused on the 204 putative oncoPPIs connecting E3 ligases using subject matter expertise based on a combination of factors: i) strong prediction from oncoPPI mutations on E3 ligases or their substrates; ii) significant association with patient survival rates; and iii) significant association with drug responses measured in tumor cell lines or patient-derived tumor xenograft (PDX) mouse models (Table S7).

Figure 6A illustrates the selected examples of the most significant PIONEER-predicted oncoPPIs of E3 ligases (Table S8). Among 204 putative oncoPPIs of E3 ligases, FBXW7 (F-box with 7 tandem WD40) has the greatest number of oncoPPIs (47/204; Figures 6A and S10; Table S9). FBXL17 (F-box/LRR-repeat protein 17) is a multiple-RING E3 ligase that specifically recognizes and ubiquitinates the BTB proteins (Mena et al., 2018). We found that PIONEER-predicted PPI-perturbing mutations of FBXL17-KEAP1, such as p.Ser102Leu on KEAP1, were significantly associated with poor survival in non-small cell lung cancer (P = 1.6 x 10^{-13}; Figure 6B). A multiple-RING E3 ligase complex ANAPC1-ANAPC2 (Figure 6A) is positively regulated by the PTEN/PI3K/AKT pathway and modulates ubiquitin-dependent cell cycle progression (Wang et al., 2003). We found that PIONEER-predicted PPI-perturbing mutations on ANAPC1-ANAPC2 is associated with resistance to a PI3K inhibitor BKM120 (P = 0.0043; Figure S11A). ITCH, a HECT-type E3 ubiquitin ligase, has been reported to mediate BRAF kinase poly-ubiquitination and promote proliferation in melanoma cells (Yin et al., 2020). We found that PIONEER-predicted PPI-perturbing mutations of BRAF-ITCH, such as p.Val600Glu and p.Lys601Glu on BRAF, are significantly associated with sensitivity to dabrafenib (an

ATP-competitive inhibitor; $P = 1.7 \times 10^{-21}$; Figure S11B). STUB1, a U-box-dependent E3 ubiquitin ligase, has been reported to degrade SMAD4, an intracellular signaling mediator of the TGF-β pathway (Li et al., 2004). Multiple PIONEER-predicted PPI-perturbing mutations of STUB1-SMAD4, including p.Gly419Arg (Trp, Val) and p.Leu540Pro (Arg) on SMAD4, are significantly associated with poor survival rate in colorectal cancer ($P = 0.025$; Figure S11C). A single-RING E3 ligase TRIM24 is an oncogenic transcription cofactor overexpressed in breast cancer (Tsai et al., 2010). We found that PIONEER-predicted PPI-perturbing mutations of TRIM24-H3C1 (Figure 6A) are significantly associated with resistance to GDC0941 (an EGFR signaling inhibitor; $P = 0.028$; Figure S11D). Treatment with an EGFR inhibitor suppresses TRIM24 expression and H3K23 acetylation and thereby inhibits EGFR-driven tumor growth (Lv et al., 2017) , supporting the PIONEER-predicted oncoPPI findings.

KEAP1 is an adapter of E3 ligase that senses oxidative stress by mediating degradation of NFE2L2/NRF2, a key transcription factor in multiple cancer types (Cuadrado et al., 2019) . Patients with non-small cell lung cancer harboring PIONEER-predicted oncoPPI mutations on NRF2 have significantly worse survival than the WT ($P = 0.029$, Figure 6C). KEAP1 recognizes NRF2 structurally through its conserved ETGE (aa 79-82) and DLG (aa 29-31) motifs (Fukutomi et al., 2014; Furukawa and Xiong, 2005). We experimentally confirmed the association of NRF2 mutations and WT KEAP1 by Co-immunoprecipitation. As shown in Figure 6D, p.Thr80Lys and p.Glu79Lys mutations on the NRF2 ETGE motif (Figure 6A) reduce the binding of NRF2 to KEAP1, whereas the p.Leu30Phe mutation on the NRF2 DLG motif partially sustains the binding of NRF2 to KEAP1. The mutation of p.Thr80Lys releases NRF2 from association with KEAP1 and

protects NRF2 from ubiquitination and subsequent degradation. We next tested whether p.Thr80Lys on NRF2 contributes to the proliferation of non-small cell lung cancer cells. A pro-proliferative effect of p.Thr80Lys was observed in a colony formation assay (Figures 6E-6F). Overexpression of WT and p.Thr80Lys NRF2 promoted the growth of the non-small cell lung cancer H1975 cell line harboring WT KEAP1 (Figure 6G). In summary, PIONEER-predicted oncoPPI-perturbing tumor alleles that alter ubiquitination by E3 ligases are significantly associated with patient survival, drug responses, and *in vitro* tumor growth.

Pharmacogenomic landscape of the PIONEER-predicted oncoPPIs

We next turned to inspect correlation between potential oncoPPIs and drug responses using high-throughput drug screening data (Figure 7A). The datasets we used include the drug pharmacogenomic profiles of >1,000 cancer cell lines and ~250 FDA-approved or clinical investigational agents from the Genomics of Drug Sensitivity in Cancer (GDSC) database and *in vivo* compound screens using ~1,000 PDX models to assess patient responses to 62 anticancer agents (Gao et al., 2015) . For each pair of oncoPPI and compound, the drug response characterization IC_{50} vector was correlated with the mutation status of the oncoPPIs using a linear ANOVA model. Figure 7B shows the landscape of the correlations between PPIs and 56 clinically investigational or approved anti-cancer drugs. In total, we identified 4,473 interface mutations that have significant correlations with drug sensitivity/resistance. Among the most significant correlations from PDX models, we found that PIONEER-predicted CDK6-BECN1 interface mutations was associated with resistance to treatment using a BYL719 plus encorafenib drug

combination, while the mutations in PIONEER-predicted BRAF-MAP2K3 interfaces (e.g., interface mutations p.Val600Glu on BRAF and p.Arg152Gln on MAP2K3, both found in bladder urothelial carcinoma and glioblastoma) conferred significant drug sensitivity to encorafenib plus binimetinib treatment (Figure 7C). In addition, we found significant drug resistance to trastuzumab and BYL719 among those cases harboring mutations in PIONEER-predicted STK4-DDIT4L (e.g., p.Arg181Gln on STK4) and ORC4-MTUS1 (e.g., p.His166Tyr on ORC4) interfaces, respectively (Figure 7C). Taken together, PIONEER-predicted PPI interface mutations can significantly affect drug sensitivity/resistance in antitumor treatment using both cancer cell lines and PDX models (Table S9).

Proteogenomic perturbation by PIONEER-predicted interface mutations

Recent proteogenomic study showed that somatic mutations altered protein or phosphoprotein abundance and further correlated with drug responses or cancer patient survival rate (Vasaikar et al., 2019). We next inspected whether PIONEER-predicted interface mutations more likely influence protein abundances in colon adenocarcinoma (COAD) and Uterine Corpus Endometrial Carcinoma (UCEC). The abundance of phosphoproteins was quantified using the tandem mass tag (TMT) assays by The National Cancer Institute's Clinical Proteomic Tumor Analysis Consortium. We found that PIONEER-predicted interface mutations significantly reduced phosphoprotein abundances in both COAD (P = 0.018) and UCEC (P = 0.001) (Figure 8A).

We next turned to inspect how the phosphorylation-associated PPI mutations identified by PIONEER perturb EGFR-RAS-RAF-MEK-ERK signaling networks in COAD (Figure 8B; Table S10). The mutations involved in this signaling cascade have been

suggested to regulate oncogenesis in colon and other cancers (Abi-Habib et al., 2005; Roberts and Der, 2007). EGFR dimerization was activated by EGF in the extracellular domain (PDB IDs:3NJP and 2M20; Figure 8B) (Endres et al., 2013; Lu et al., 2010). Binding of EGF triggers conformational changes in the C-terminal domain (PDB: 2GS6) (Liang et al., 2018) and results in autophosphorylation of specific tyrosine residues, such as Tyr1068 (Bishayee et al., 1999). The C-terminal domain of EGFR is essential for adapter protein binding to initiate signal transduction, such as by mediating GRB2/SOS1 (Siegelin and Borczuk, 2014). Via PIONEER, we identified that two mutations, p.Thr1021Ile and p.Thr1074Ile on EGFR C-terminal domain, may alter the phosphorylated PPI interaction with downstream adapter protein of SOS1 (Figure 8B). SOS1, a RAS activator, which, by loading GTP, was reported to interact allosterically with the Ras/Ras p.Gly12Cys mutant (PDB: 6EPO) (Hillig et al., 2019). SOS1 deficiency attenuates KRAS-induced leukemia in mouse model (You et al., 2018). A selective SOS1–KRAS PPI inhibitor, BI 1701963, has been developed for advanced KRAS-mutated solid tumors in a Phase 1 clinical trial (Hofmann et al., 2021b) . Using PIONEER, we identified two SOS1-KRAS PPI perturbation mutations, including p.Tyr884His on SOS1 and p.Gln61His on KRAS (Figure 8B). Specifically, Tyr884 and Gln61 have strong hydrogen bond and cation-π interaction between KRAS and SOS1. We pinpointed that PIONEER-predicted SOS1–KRAS interface mutations are significantly related to trametinib resistance compared to WT group ($P = 7.6\times10^{-12}$; Figure 8C), offering potential pharmacogenomic biomarkers for trametinib (a MEK inhibitor) in KRAS-mutant colorectal cancer (Huijberts et al., 2020) . Binimetinib, another MEK-selective inhibitor (Cho et al.,

2017), is significantly associated with resistance in PDX models harboring PIONEER-predicted SOS1–KRAS interface mutations (*P* = 0.0044; Figure 8C).

GTP-bound active RAS recruits RAF proteins (e.g., RAF1 and BRAF) to the plasma membrane to orchestrate MAPK signaling (Hofmann et al., 2021a). Figure 8B shows PPIs of both KRAS-RAF1 and KRAS-BRAF constructed in one structure complex. Oncogenic mutations on KRAS, such as p.Gly12Val, p.Gly13Asp, and p.Gln61Leu, are the most frequent mutations in common tumors (Liu et al., 2018). PIONEER-predicted interface mutations of KRAS-RAF1 N-terminal, such as p.Arg59Ala and p.Asn64Ala on RAF1, are associated with a significantly reduced binding affinity of the PPI (Tran et al., 2021), but not oncogenic mutations p.Gly12Val and p.Gly13Asp on KRAS (PDB ID: 6VJJ; Figure 8B). In addition, we identified PIONEER-predicted KRAS-BRAF interface mutations are significantly associated with resistance of a MEK inhibitor refametinib (Patelli et al., 2021) ($P = 4.7 \times 10^{-27}$; Figure 8C).

The key step for triggering the signaling cascade is that RAS-induced RAF dimerization subsequently phosphorylates MEK1/2 protein kinases (Roberts and Der, 2007). Of RAF family members, BRAF shows the most potent activity (Liu et al., 2018) and the BRAF p.Val600Glu mutation confers a poor survival and prognosis in colorectal cancer (Corcoran et al., 2018; Li et al., 2020). Via PIONEER, we identified two PPI interface mutations, p.Gly466Val and p.Asn581Ser on BRAF, may mediate how BRAF coordinates MEK1 by its C-lobes in the kinase domain (Figure 8B), consistent with a previous study (Lin et al., 2019). Considering that the E3 ligase ITCH is also involved in BRAF regulation and binding to the kinase domain (Figures 6A), we identified that PIONEER-predicted interface residue of Val600 on BRAF may perturb interaction

between BRAF and ITCH (Figure 8B). Phosphorylated MEK1 acts as upstream activators to phosphorylate ERK1/2 kinase activities in the MAPK cascade (Caunt et al., 2015). PIONEER-predicted interface mutation of p.Asp179Asn on ERK1 alter MEK1-ERK1 signaling network (Figure 8B) (Huang et al., 2019). In summary, we showed that PIONEER-predicted oncoPPIs could characterize proteogenomic alterations in the EGFR-RAS-RAF-MEK-ERK signaling pathways in colon cancer and other cancer signaling pathways if broadly applied.

Construction of the 3D structural interactome web server

In total, our 3D interactomes cover all 282,095 experimentally determined binary interactions in the literature for humans and seven other commonly studied organisms, including all 146,138 experimentally determined human interactions (Figures 1A and 2A). The web server is a user-friendly tool for genome-wide protein functional exploration through which users can identify functionally enriched areas of protein interactomes and browse multi-scale structural interactome networks (Figure S12). It utilizes the PIONEER framework to provide seamlessly rapid on-demand predictions for user-submitted interactions. The web tool also contains 161,244 disease-associated mutations across 10,564 disorders in HGMD and ClinVar (Landrum et al., 2016) with their per-disease enrichment pre-computed on protein interaction interfaces with 3D spatial clustering at atomic resolution for interacting protein pairs with structure models, and at the residue and domain levels for those without structures. By providing a user-friendly tool to visualize each protein and its given interactors with all available domain information, co-crystal structures, homology models, and PIONEER-predicted interfaces coupled with all

known disease mutation information, PIONEER seamlessly allows users to explore the effect of mutations on 3D structures. We believe that the PIONEER web server will be instrumental in uncovering novel discoveries in relationships among these mutations with regards to the study of disease mechanisms and corresponding personalized treatment in cancer or other diseases if broadly applied.

DISCUSSION

The systematic characterization of 3D protein-protein interactome network models from individual protein sequences and structures remains a major challenge in network medicine and is of the utmost practical and theoretical importance (Braberg et al., 2022; Chowdhury et al., 2022). The structural models of protein interactions can be experimentally determined through resource-intensive and time-consuming X-ray crystallography, NMR, and more recently, cryo-EM experiments. Computational methods, such as docking and homology modeling, have been developed to predict PPI interfaces. Although docking methods can achieve atomic resolution, they do not generally behave well especially in cases where proteins undergo large conformational changes (Afsar Minhas et al., 2014; Sanchez-Garcia et al., 2019). Homology modeling, which covers only another ~3% of interactions, infers protein interfaces from templates of homologous complexes (Xue et al., 2015). To date, ~91% of PPIs still do not have structural information. Hence, most network studies model proteins as graph-theoretical nodes, which ignores the structural details of the individual proteins as well as the spatial constraints of their interactions.

We previously developed the innovative ensemble random forest-based pipeline, ECLAIR, which was among the first to generate the full-proteome 3D human interactome network. Over the last several years, deep learning techniques have shown exceptional representation learning abilities and much improved performance, especially in processing 3D protein structures (Lee et al., 2022), compared to traditional machine learning algorithms, including random forest. A number of methods (Fout et al., 2017; Townshend et al., 2019; Tubiana et al., 2022), therefore, have been proposed that have gained considerable traction for protein interface prediction. However, a major limitation of these methods is that they do not leverage the notable combination of feature representations indicated in both structures and sequences well nor do they effectively integrate embeddings from both the local regions of target residues and the whole proteins, thereby leaving much room for improvement in prediction quality. Recently, RoseTTAFold (Baek et al., 2021) and AlphaFold2 (Jumper et al., 2021) have made a significant breakthrough in generating single protein structural models from solely protein sequences, which is extremely helpful for protein interactome studies. Even more recently, AlphaFold-Multimer (Evans et al., 2022) has generated structural models for multi-chain protein complexes also using only protein sequences. Although AlphaFold-Multimer can be used to generate good models for protein interactions, it is very computationally intensive, and, thus, cannot be scaled to generate models for the hundreds of thousands of interactions in whole interactomes. And a recent study has shown that AlphaFold2 can successfully generate high-quality models for only ~2% of interactions without known homologous structure (Burke et al., 2023).

Here, we present a comprehensive, multiscale 3D interactome framework and web server, which we named PIONEER, to combine seamlessly genomic-scale data with structural proteomic analyses. This resource is based on our deep-learning-based ensemble framework, which accurately predicts partner-specific interaction interfaces for all protein-protein interactions in humans and seven other common model organisms. We found PIONEER outperforms other existing state-of-the-art methods, including our previously developed method, ECLAIR. Moreover, large-scale statistical analysis and mutagenesis experiments show that PIONEER-predicted interfaces reveal similar biological significance as those of known interfaces in the PDB. Further analysis shows that interactome PIONEER plays a pivotal role in dissecting the pathobiology of diseases. Our work is implemented as both a web server platform and a software package to help facilitate systematic structural analysis in genomic studies, thereby allowing the wider scientific community to adopt and further develop upon our PIONEER framework.

With the rapid advances in sequencing technologies, multiple whole genome/exome sequencing projects are currently being carried out, including TCGA, cardiovascular medicine (i.e., National Heart, Lung and Blood Institute's Trans-Omics for Precision Medicine program (Taliun et al., 2021)), and Alzheimer's disease sequencing project (Gary et al., 2017), to identify trait/disease-associated genes and mutations. Although the 3D structure of each protein fundamentally determines its function, systematic structural analysis is currently not part of any major genomic study pipeline. One of the main reasons for this disconnection is the poor coverage of atomic-resolution structural models of proteins and their interactions. We expect our comprehensive 3D interactomes generated by PIONEER, which provides high-quality partner-specific

interfaces on the scale of the whole interactome, will help bridge the gap between genome-scale data and structural proteomic analyses. With the high-quality and comprehensive map of protein interfaces, there are numerous valuable extensions considering the biophysical effects induced by mutations at protein interfaces, such as the investigation of disease etiology and the corresponding drug prioritization, and prediction of specific disease pathobiology. The partner-specific property of PIONEER-generated 3D interactomes also allows us to study the pleiotropic effects of genes. Therefore, the powerful and comprehensive PIONEER framework will make such extensive research possible, and, more importantly, provide potentially unforeseen avenues for drug design and therapeutics.

We have not only implemented PIONEER and the resulting multiscale 3D interactomes into a user-friendly web server platform, but also constructed the PIONEER framework as a flexible software package, which benefits users and developers as well. We demonstrated PIONEER's utility in discovering new biological insights into multiple genome medicine studies. We combined PIONEER predictions along with co-crystal structures and homology models to reconstruct a subnetwork in the human interactome that is enriched with disease mutations. Specifically, we demonstrated the PIONEER-predicted interface mutations significantly enriched in both somatic cancer and germline mutations. Moreover, PIONEER-predicted interface mutations highly correlated with cancer patient survival rate and anti-cancer responses in both tumor cell lines and PDX models. In addition, we experimentally validated PIONEER-predicted PPI interface mutations using CCND1-CDK4 and KEAP1-NRF2 as two examples. In particular, PIONEER-predicted PPI interface mutation altering E3 ligase between significantly

promoted non-small cell lung cancer cell growth. In summary, these comprehensive observations illustrated high clinical utility of the PIONEER-predicted 3D structural interactome networks in genome research and precision medicine studies.

The web server platform allows for a broad range of investigations related to protein interfaces on a genome-wide scale while also carrying out on-demand interface predictions for user-uploaded interactions. Furthermore, the software package increases the utilization, maintenance, and further development of PIONEER by the wider scientific community. The accompanying web portal, containing all relevant PDB structures and homology models, as well as predicted interface residues and domains, significantly reduces the barrier-to-entry to perform systematic structural analysis for most genetics/genomics researchers, and allows for implementing such analyses (e.g., looking for enrichment of mutations on protein structures and interfaces at various resolutions, distinguishing mutations in different interfaces of the same protein) in genome/exome sequencing projects. Additionally, the continually updated and extendable software package bears great potential for stimulating the adoption and development of our PIONEER framework for related genome medicine research.

DATA AND CODE AVAILABILITY

The main data supporting the results in this study are available within the paper, its supplementary information, and at https://pioneer.yulab.org. The source code of PIONEER is available at https://github.com/hyulab/PIONEER. Additional data files and codes that support the findings of this study is available from the corresponding authors upon request.

ACKNOWLEDGMENTS

This work was supported by the National Institute on Aging (NIA) under Award Number U01AG073323, R01AG076448, R01AG082211, R01AG066707, and R56AG074001 to F.C.; the National Institute of General Medical Sciences (R01GM124559, R01GM125639, R01GM130885, and RM1GM139738) and The National Institute of Diabetes and Digestive and Kidney Diseases (R01DK115398) to H.Y.; and the National Human Genome Research Institute (U01HG007691), the National Heart, Lung, and Blood Institute (R01HL155107, R01HL155096, and U54HL119145), the American Heart Association (AHA957729), and European Union Horizon Health 2021 (101057619) to J.L. C.E. is the Sondra J. and Stephen R. Hardis Chair of Cancer Genomic Medicine at the Cleveland Clinic.

AUTHOR CONTRIBUTIONS

D.X., J.Z., Y.Q., Y.Z., D.L., S.G., F.C. and H.Y. conceived and developed the project. D.X., D.L. and S.L. developed the models and conducted computational experiments. S.G. and S.L. built the web server. W.L., J.K. conducted biological experiments. D.X., J.Z., Y.Q., Y.Z., D.L., F.C. and H.Y. performed the analyses. D.X., J.Z., Y.Q., Y.Z., D.L., S.G., C.E., J.L., F.C. and H.Y. wrote and critically revised the manuscript. All authors discussed the results and reviewed the manuscript.

DECLARATION OF INTERESTS

J.L. (Joseph Loscalzo) is co-scientific founder of Scipher Medicine, Inc., which applies network medicine strategies to biomarker development and personalized drug selection. The remaining authors declare no competing interests.

Figure Legends

Figure 1. Overview of the PIONEER framework

(A) The current size of protein-protein interactions from the eight common model organisms with the coverage of experimentally determined co-crystal structures, homology models, and the unresolved interactions.

(B) The partner-specific interactions are prioritized in our training dataset for solving partner-specific interface prediction.

(C-F) PIONEER architecture consists of an ensemble of four deep learning models that ensures every residue in the interactomes can be predicted with the maximal amount of available information, and uses a comprehensive set of 30 biophysical, evolutionary, structural, and sequence features for in-depth feature characterization. The (C) and (D) models represent interactions in which both proteins and neither protein has structural information available, respectively. The GCNs and RNNs are used for structure and sequence information embeddings, respectively. The (E) and (F) models represent interactions in which only one protein has structure information available. The transfer learning was used in (E) and (F), specifically, the pre-trained GCNs-RNNs in (A) and RNNs in (B) are deployed in (C) and (D).

Figure 2. PIONEER provides high-quality interfaces for the whole proteome

(A) Workflow for compiling interactome PIONEER. The interfaces calculated from experimentally determined co-crystal structures or homology models are primarily used; the remaining unresolved interactions are predicted by PIONEER.

(B) Fraction of interactions disrupted by random population variants in PIONEER-predicted and known interfaces.

(C-D) Comparison of receiver operating characteristic (ROC) (C) and precision-recall (PR) (D) curves of the PIONEER Structure-Structure and Sequence-Sequence models with other state-of-the-art structure-based methods. See also Table S2.

(E-F) Comparison of ROC (E) and PR (F) curves of the PIONEER Sequence-Sequence model with other state-of-the-art sequence-based methods. See also Table S3.

Figure 3. PIONEER-predicted PPI alleles are enriched in disease-associated mutations

(A) Enrichment of disease mutations in PIONEER-predicted and known interfaces. Significance was determined by two-tailed Z-test.

(B) Enrichment of population variants in PIONEER-predicted and known interfaces. Predicted deleteriousness of population variants in PIONEER-predicted and known interfaces using PolyPhen-2.

(C) Distribution of mutation burden at protein–protein interfaces for disease-associated germline mutations from HGMD in comparison with mutations from the 1KGP and ExAC. Significance was determined by two-proportion Z-test.

(D) PPI network with disease-associated interface mutations. Disease associations of the interface mutations were extracted from the HGMD database. Using the PIONEER-predicted high-confidence interface information, PPIs that have at least one disease-associated interface mutation from either one of the two interacting proteins were included in the network. Node colors were determined by the disease categories of their disease-associated interface mutations. Interacting proteins with no known disease-associated interface mutations were colored as “Neighbor.” The final network contains 10,753 PPIs among 5,684 proteins. The figure shows the largest connected component of the network that has 10,706 edges and 5,605 nodes. See also Table S6.

(E) Selected structural complex pairs showing germline mutations in the PPI interface. Three disease associated PPIs with mutations are shown: LMNA-BAF (PDB: 6GHD), PPIA-SYUA (PDB: 6I42), and VHL-HIF-2α (PDB: 6BVB). The surface of proteins in complex are shown in blue and wheat. Mutations are shown in green.

Figure 4. A landscape of oncoPPIs identified by PIONEER across 33 cancer types (~11,000 cancer genomes)

(A) Distribution of missense somatic mutations in protein–protein interfaces versus non-interfaces across 33 cancer types/subtypes from TCGA. The data are represented as violin plots with underlaid boxplots, where the middle line is the median, the lower and upper edges of the rectangle are the first and third quartiles, and the lower and upper

whiskers of the violin plot represent the interquartile range (IQR) × 1.5. Significance was determined by two-tailed Wilcoxon rank-sum test.

(B) Circos plot displaying significant putative oncoPPIs harboring a statistically significant excess number of missense somatic mutations at PPI interfaces across 33 cancer types. Putative oncoPPIs with various significance levels are plotted in the three inner layers. The links (edges, orange) connecting two oncoPPIs indicate two cancer types sharing the same oncoPPIs. Selected significant oncoPPIs and their related mutations are plotted on the outer surface. The length of each line is proportional to $-\log_{10}(P)$.

Figure 5. PIONEER-predicted oncoPPIs are associated with patient survival

(A) Selected structural complex pairs showing somatic mutations in the oncoPPI interface.

(B) Survival analysis of six exemplary PPI perturbing mutations in diverse cancer types. Significance was determined by log-rank test.

(C) Example of PIONEER partner-specific interface prediction. The mutations CCND1 p.Lys114Arg and CCND1 p.Glu162Lys are shown in green and pink, respectively.

(D) Experimental validation of the partner-specific interface prediction in (C) by co-immunoprecipitation using HEK293T cells.

Figure 6. PIONEER-predicted PPI-perturbing tumor alleles in ubiquitination by E3 ligases

(A) A landscape of six E3 complexes with PPI perturbing mutations. The complex or single protein models from PDB or PIONEER modeling are shown. The protein in wheat denotes the E3 ligase, while the protein in blue denotes the specific substrate of E3 ligase. Interface mutations are denoted in green. See also Table S8.

(B-C) Interface mutations of KEAP1-FBXL17 (B) and KEAP1-NRF2 (C) are significantly correlated with survival rate in non-small cell lung cancer. Significance was determined by log-rank test.

(D) Experimental validation of mutation effects of p.Thr80Lys and p.Glu79Lys on the NRF2 ETGE motif, and p.Leu30Phe on the NRF2 DLG motif on the interactions between KEAP1 and WT NRF2 were determined by co-immunoprecipitation with HEK293T cells.

(E-F) Colony formation assay of H1975 cells transfected with NRF2 p.Thr80Lys, NRF2 WT expressing vectors, and empty vectors. Relative growth index was analyzed with ImageJ software (Schneider et al., 2012).
(G) Growth curves of H1975 cells transfected with NRF2 p.Thr80Lys, NRF2 WT expressing vectors, and empty vectors, at day 4.

Figure 7. Pharmacogenomic landscape identified by the PIONEER-predicted interactome network

(A) Drug responses evaluated by oncoPPIs in the PDX models. Effect size was quantified by Cohen's *d* statistic using the difference between two means
divided by a pooled s.d. for the data.
(B) Circos plot displaying drug responses evaluated by putative PIONEER-predicted oncoPPIs harboring a statistically significant excess number of missense mutations at PPI interfaces, following a binomial distribution across selected anticancer therapeutic agents in cancer cell lines. Each node denotes a specific oncoPPI. Node size denotes significance determined by ANOVA. Effect size was quantified by Cohen's *d* statistic using the difference between two means divided by a pooled s.d. for the data. Node color denotes three different types of PPIs: (1) Experimental: Red; (2) HM: Blue; and (3) PIONEER: Green.
(C) Highlighted examples of drug responses. Values were calculated using ANOVA. Data are represented as a boxplot with an underlaid violin plot in which the middle line is the median, the lower and upper edges of the box are the first and third quartiles, the whiskers represent IQR × 1.5, and beyond the whiskers are outlier points. Significance was determined by ANOVA.

Figure 8. Proteogenomics of the PIONEER-predicted interactome network

(A) Phosphorylation-associated PPI perturbing mutations altered the proteomic changes in COAD and UCEC. The abundance of proteins was quantified using the TMT technique. Significance was determined by two-tailed Wilcoxon rank-sum test.
(B) Phosphorylation-associated PPI perturbing mutations in the EGFR-RAS-RAF-MEK-ERK cascade signaling pathway. The whole transmembrane EGFR structures were

constructed by three crystal structures (PDB: 3NJP, 2M20, 2GS6). The membrane model is shown in green. The phosphorylation sites are indicated by the “P” symbol. The detailed interface structure of SOS1-KRAS is also shown in the inset. The key mutated residue Gln61 on KRAS forms a hydrogen bond (purple dashed line) with residue Thr935 on SOS1, and Tyr884 on SOS1 is involved in a cation-π interaction (red dash line) with residue Arg73 on KRAS. Two subunits of RAF protein structure models were built by RAF1 and BRAF, separately (PDB: 6VJJ and 6Q0J). The two subunits are connected by a disordered loop indicated by blue cartoon lines. Two heterodimers of KRAS-RAF1 and BRAF-MEK1 constitutes the KRAS-RAF-MEK1 complex. PDB ID of each complex structure model is provided. See also Table S10.

(C) Highlighted examples of responses to the MEK inhibitor drugs trametinib for KRAS-SOS1 mutations (n = 103 mutated cell lines, n = 827 WT cell lines), refametinib for KRAS-BRAF mutations (n = 179 mutated cell lines, n = 1,610 WT cell lines), and binimetinib for KRAS-SOS1 mutations in the PDX models (n = 62 mutated samples, n = 166 WT samples). Significance was determined by ANOVA.

Supplementary Materials

Figures S1-S12

Tables S1-S10

Datasets S1-S3

METHOD DETAILS

PPI data construction

We compiled 282,095 binary interactions for *H. sapiens, A. thaliana, S. cerevisiae, D. melanogaster, C. elegans, M. musculus, S. pombe and E. coli* in total, including 9,123 full experimentally determined binary interactions in humans. The interactions with known co-crystal structures in the PDB were used to form the training, validation, and testing datasets to build PIONEER models, which then predicted the interfaces for all the other interactions without known co-crystal or homologous structures.

We calculated the partner-specific interface residues for those interactions with known co-crystal structures in the PDB. SIFTS (Velankar et al., 2013) was then used to map the UniProt-indexed residues to the PDB-indexed residues. To determine the interface residues, we used NACCESS (Lee and Richards, 1971) to assess the change in solvent-accessible surface area of the protein in complex and in isolation. Specifically, an interface residue is defined as a residue that is a surface residue (≥15% exposed surface) with its SASA decreasing by ≥1.0Å^2 in the complex. We reviewed all available structures in the PDB for an interaction, and considered a residue to be in the interface of that interaction if it had been calculated to be an interface residue in at least one of the corresponding co-crystal structures. By only considering interactions for which aggregated co-crystal structures have been combined to cover at least 30% of the UniProt residues for both interacting proteins, the training, validation, and independent benchmark testing datasets were built, which included a random selection of 2,615, 400, and 400 interactions with known co-crystal structures, respectively. Additionally, we ensured that no homologous interactions or repeated proteins existed between any of the two datasets to guarantee the robustness and generalizability of our models, and a fair performance evaluation.

Feature characterization

Our previous pipeline ECLAIR employed a set of representative feature groups to describe the residues, including biophysical residue properties, evolutionary sequence conservation, co-evolution, SASA, and docking-based metrics. While retaining all features from ECLAIR here, we also implemented two new feature groups to seek a more

comprehensive and in-depth feature characterization. From each feature group, we synthesized a variation of features using scaling, by which we mean that each feature used its raw calculated values and normalized values against the average of all positions per protein.

1. *Predicted protein structural properties*: Here, in addition to SASA used in ECLAIR, we also used RaptorX (Wang et al., 2016) to predict the solvent accessibility state (buried, medium, and exposed) and the secondary structure state (helix, strand, and coil), which are especially useful for proteins without structure information. The predicted solvent accessibility and secondary structure were represented by their predicted probabilities.
2. *Pair potential*: In our previous ECLAIR, we used co-evolution and docking-based features to describe this partner-specific issue, which, however, is not available for the interactions not having co-evolution and structure information, respectively. Although our deep learning architectures solve this problem by considering the partner protein embedding derived from the inputs, here, inspired by the pairing preferences at protein-protein interfaces proposed by Glaser et al. (Glaser et al., 2001), we also proposed a novel feature, pair potential, to specifically characterize the interface propensity for the target protein with respect to its respective partner. Pair potential was developed solely based on sequence information so it can be applied to all the binary protein interactions. To calculate pair potential, we need first to calculate the propensity matrix *G* of contacting residue pairs:

$$G_{ij} = log(Q_{ij}/(W_i * W_j)),$$

$$Q_{ij} = C_{ij} * V_i * V_j / \Sigma_{i,j(i \leq j)}(C_{ij} * V_i * V_j),$$

$$W_i = N_i / \Sigma N_i \ ,$$

where Q_{ij} is the normalized number of contacting residue pairs between residues *i* in the target protein and *j* in the partner protein, C_{ij} is the number of contacting residue pairs observed between residues *i* and *j*, V_i is the volume of residue *i*, W_i is the normalized frequency of interfaces, and N_i is the number of interface residues *i* from both target and partner proteins. The propensity matrix *G* was calculated using only interface residues in our training dataset. The pair potential for each residue in the target protein can, thus, be calculated as:

$$P_i = \Sigma_j (G_{ij} * F_j),$$

where F_j is the frequency of residue j in the partner protein.

Model building

In order to ensure that every residue is meticulously predicted through the maximal amount of available information from both proteins in an interaction pair, we built four deep learning models in which each model takes different interactions as input based on the availability of structures.

1. Structure-Structure model (Figures 1A, S1A, and S2): For interactions where both proteins have structural information available, the structure and sequence information were embedded through GCNs with ARMA filters and bidirectional RNNs with GRUs, respectively. Specifically, GCN utilizes the structure information from graph representations of protein structures where each node represents a residue, and each edge signifies that two residues are adjacent. For each node, GCN incorporates its spatial neighborhood information to generate a more comprehensive residue representation whereas RNN explores amino acid sequences to include the sequential neighborhood information of each residue. The RNN extracts the upstream and downstream sequence information from each residue. Through the concatenation and mean aggregation, the residue embeddings of both target protein and partner protein were then converted to protein embeddings, respectively. Finally, the residue embeddings, target protein embedding, and partner protein embedding were concatenated and fed into the fully connected layers to make prediction for each residue in the target protein.
2. Sequence-Sequence model (Figures 1B, S1B, and S2B): For interactions where neither protein has structure information, the sequence information of both proteins was fed into the RNNs. Next, in a manner similar to that described in the Structure-Structure model, the residue embeddings, target protein embedding, and partner protein embedding were concatenated and fed into the fully connected layers to make prediction for each residue in the target protein.
3. Structure-Sequence and Sequence-Structure models (Figures 1C-1D, S1C-S1D, and S2): The use of Structure-Sequence or Sequence-Structure model depends

on whether target protein or partner protein has structure information, respectively. The transfer learning was used in these two models, which means the pre-trained GCNs-RNNs in the above Structure-Structure model and RNNs in the above Sequence-Sequence model were deployed in the Structure-Sequence model and the Sequence-Structure model for the processing of proteins with and without structure information, respectively. Subsequently, in a manner similar to that described in the Structure-Structure model and Sequence-Sequence model, the residue embeddings, target protein embedding, and partner protein embedding were concatenated, and fed into the fully connected layers to make prediction for each residue in the target protein.

We compiled a set of representative protein structures from the PDB and ModBase (Pieper et al., 2014) for each protein. For ModBase models, we only consider the models with a ModPipe Quality Score (MPSQ) ≥1.1. The structures were sorted by the coverage of UniProt residues based on SIFTS, excluding any homologous PDB structures of interacting protein pairs. Each residue in a target protein was then reviewed if it has structure information; if so, it was predicted using that protein's first corresponding structure which contains the structure information of that residue; otherwise, it was predicted using the sequence information. For the partner protein which has structure information, we only used the corresponding structure with the highest UniProt coverage.

Our PIONEER framework was implemented using PyTorch. To maximize model performance, we carried out comprehensive hyperparameter optimization for the neural network architectures, and the optimal set of hyperparameters were determined by maximizing the AUROC on the validation set. All four models were trained with cross entropy loss and the Adam optimizer; the kernel activation function (Scardapane et al., 2019) was used in GCNs and fully connected layers. The hyperparameters used for these four models can be found in our accompanying PIONEER software package. To solve the variable length inputs, we trained all four models in a mini-batch mode with only a single protein pair.

Performance evaluation

After identifying the best hyperparameters for each model, a thorough examination was performed using the benchmark testing set. Models were ordered based on their AUROCs on the validation set, which means the priorities of models are Structure-Structure, Structure-Sequence, Sequence-Structure, and Sequence-Sequence, respectively. For the overall performance, the raw prediction score of each residue was taken from the results of the model with highest priority according to the availability of structures of the target protein containing that residue and its partner protein. We further compared PIONEER with a number of existing state-of-the-art methods, including ECLAIR, ScanNet, BIPSPI+, DeepPPISP, SASNet, PIPGCN, DELPHI (Li et al., 2021a), SCRIBER (Zhang and Kurgan, 2019), and DLPred (Zhang et al., 2019). We also reported performance metrics at various discrete and comparable levels of confidence, which consist of Very low, Low, Medium, High, and Very high prediction categories, by evenly separating into fifths our raw prediction scores.

Interface prediction

By further incorporating AlphaFold2-predicted structures, we predicted interface residues for the remaining 256,946 interactions not resolved by either PDB structures or homology models. Each residue was then predicted by the model of the ensemble with the highest priority according to the availability of structures of the target protein containing that residue and its partner protein.

Mutagenesis validation experiments

We performed mutagenesis experiments where we introduced random human population variants from the Exome Sequencing Project (Fu et al., 2013) into predicted interfaces, known interfaces, and non-interfaces. We randomly selected mutations of predicted interfaces in each of the PIONEER prediction categories (very low – very high). We also selected random mutations of known interfaces and non-interfaces in co-crystal structures in the PDB as positive and negative controls. The selected mutations were introduced into the proteins according to our Clone-seq pipeline (Wei et al., 2014). We generated 2,395 mutations on 1,141 proteins and examined their impact on 6,754

mutation-interaction pairs (either disrupting or maintaining the interactions) using our high-throughput Y2H assay.

Y2H assay

Y2H was performed as previously described (Meyer et al., 2018). Gateway LR reactions were used to transfer all wild-type/mutant clones into our Y2H pDEST-AD and pDEST-DB vectors. All DB-X and AD-Y plasmids were transformed into the Y2H strains MATα Y8930 and MATa Y8800, respectively. Thereafter, each of the DB-X MATα transformants (wild-type and mutants) were mated with corresponding AD-Y MATa transformants (wild-type and mutants) individually through automated 96-well procedures, including inoculation of AD-Y and DB-X yeast cultures, mating on YEPD media (incubated overnight at 30 °C), and replica-plating onto selective Synthetic Complete media lacking histidine, leucine, and tryptophan, and supplemented with 1 mM of 3-amino-1,2,4-triazole (SC-Leu-Trp-His+3AT), SC-Leu-His+3AT plates containing 1 mg/l cycloheximide (SC-Leu-His+3AT+CHX), SC-Leu-Trp-Adenine (Ade) plates, and SC-Leu-Ade+CHX plates to test for CHX-sensitive expression of the LYS2::GAL1-HIS3 and GAL2-ADE2 reporter genes. The plates containing cycloheximide were used to select for cells that do not have the AD plasmid due to plasmid shuffling. Spontaneous auto-activators (Walhout and Vidal, 2001), therefore, were identified by growth on these control plates. These plates were incubated overnight at 30 °C and “replica-cleaned” the following day. Subsequently, plates were incubated for three more days, after which positive colonies were scored as those that grow on SC-Leu-Trp-His+3AT and/or on SC-Leu-Trp-Ade, but not on SC-Leu-His+3AT+CHX or on SC-Leu-Ade+CHX. Disruption of an interaction by a mutation was defined as at least 50% reduction of growth consistently across both reporter genes when compared to Y2H phenotypes of the corresponding wild-type allele as benchmarked by 2-fold serial dilution experiments. All Y2H experiments were repeated 3 times.

Co-immunoprecipitation

The first co-immunoprecipitation assay was conducted to validate the PIONEER partner-specific interface prediction. Specially, HEK293T cells were maintained in DMEM medium supplemented 10% Fetal Bovine Serum. Cells were seeded onto 10 cm dishes and

incubated until 40-50% confluency, and were transfected with a mixed solution of 3 μg of bait construct (CCND1), 3 μg of prey construct (CDK4 or TSC2), 30 μl of 1 mg/ml PEI (Polysciences, 23966), and 1.2 ml OptiMEM (Gibco, 31085-062). After 48 hrs incubation, transfected cells were washed three times in 10 ml DPBS (VWR, 14190144), resuspended in 500 μl NP-40 lysis buffer (50 mM Tris pH 7.5, 150 mM NaCl, 5 mM EDTA, 1.0% NP-40) and incubated on the ice for 30 min. Whole lysate is sonicated on a sonifier cell disruptor (BRANSON, 500-220-180) for 120 sec at 40% amplitude. Extracts were cleared by centrifugation for 15 min at 16,100 g at 4 °C. For co-immunoprecipitation, 500 μl cell lysate per sample reaction was incubated with 15 μl of EZ view Red Anti-FLAG M2 Affinity Gel (Sigma, F2426) overnight 4 °C with a nutator. After incubation, bound proteins were washed three times in NP-40 lysis buffer and then eluted in 200 μl of elution buffer (10 mM Tris-Cl pH 8.0, 1% SDS) at 65 °C for 15 min. FLAG-co-purified samples were run on 8% SDS-PAGE gel and the proteins were transferred to PVDF membranes. Anti-FLAG (Sigma, F1804), and Anti-MYC (Invitrogen, 132500) at both 1:5,000 dilutions were used for immunoblotting analysis.

We also validated mutation effects for KEAP1-NRF2 by co-immunoprecipitation assay, in which HEK293T cells were co-transfected with WT KEP1 expressing vector and either WT NRF2, p.Thr80Lys, p.Glu79Lys, or p.Leu30Phe expressing vectors for 48 hours. Cells were lysed with NP-40 lysis buffer on ice, and supernatants were incubated with anti-HA antibody coupled with protein A/G beads (Santa Cruz,) overnight. Immunoprecipitated complexes were washed with NP-40 lysis buffer for 3 times, and were then eluted and subjected to Western blotting.

Collection and preparation of genome sequencing data

We collected variant data across multiple sources including TCGA, MSK-MET, 1KGP, ExAC, HGMD, Cancer Cell Line Encyclopedia and genomic profiling of PDXs from previous study (Gao et al., 2015). For unannotated datasets, we used VEP (McLaren et al., 2016) to annotate these variants in order to identify the corresponding amino acid changes. We regard one PPI as mutated if one variant affects the amino acid residue in the interface of either protein involved in the interaction.

Significance determination of PPI interface mutations

The significance of PPI interface mutations were tested using the method as described in our previous study (Cheng et al., 2021). A PPI in which there is significant enrichment in interface mutations in one or the other of the two protein-binding partners across individuals will be defined as an oncoPPI. For each gene g_i and its PPI interfaces, we assume that the observed number of mutations for a given interface follows a binomial distribution, binomial (T, p_{g_i}), in which *T* is the total number of mutations observed in one gene, and p_{g_i} is the estimated mutation rate for the region of interest under the null hypothesis that the region was not recurrently mutated. Using length(g_i) to represent the length of the protein product of gene g_i, for each interface, we computed the *P* value - the probability of observing >k mutations around this interface out of *T* total mutations observed in this gene - using the following equations:

$$P(X \geq k) = 1 - P(X < k) = 1 - \sum_{x=0}^{k-1} \binom{T}{x} p_{g_i}^{x} (1 - p_{g_i})^{T-x}$$

$$p_{g_i} = \frac{length\ of\ interface}{length(g_i)}$$

Finally, we set the minimal *P* value across all the interfaces in a specific protein as the representative *P* value of its coding gene g_i, denoted $P(g_i)$. The significance of each PPI is defined as the product of *P* values of the two proteins (gene products). All *P* values were adjusted for multiple testing using the Bonferroni correction.

PPI system construction of E3 ligases.

355 E3 ubiquitin ligases were retrieved and merged from E3net and Ubinet2.0. 4,613 E3s-associated oncoPPIs were analyzed after removing PPIs with homodimers or without gene name. These oncoPPIs include 198 oncoPPIs from the PDB database, 197 from Homology Models, and 4,218 from PIONEER. The correlations between mutations in E3 oncoPPIs and anticancer drug responses in TCGA cell lines, PDX models, and cancer survival rates from TCGA and MSK MetTropism datasets were then calculated (Table S9).

Complex crystal structures (PDBs: 3HQH, 3O37, 4O1V, 5G05, 5LNB, 5VZU, 6F8F, 6I68, 6M90, 6WCQ, 7K2M and 7LIO) were accessed from the RCSB PDB protein data

bank. The structures in the complex without co-crystal structures were retrieved from the AlphaFold2 portal (https://alphafold.ebi.ac.uk). PIONEER predicted PPI models were constructed using HADDOCK (Dominguez et al., 2003). The names, mutations and PDB ID were also shown in Table S8.

The linear ANOVA model

We used the drug response data of human cancer cell line from GDSC datasets and to investigate the association of PPI interface mutation with drug response. For each drug, a drug-response vector consisting of IC_{50} values was modeled using the status of a genomic feature (whether a PPI interface is mutated), the tissue of origin of the cell lines, screening medium, and growth properties by fitting a linear model. A genomic feature-drug pair was tested only if the final IC_{50} vector contained at least 10 positive cell lines. The effect size was quantified through Cohen's *d* statistic using the difference between two means divided by a pooled standard deviation for the data. The resulting *P*-values were corrected by the Benjamini-Hochberg method (Benjamini and Hochberg, 1995). Similar to cell line drug response analysis, we also used the drug response data from high-throughput screening using PDX models to study the association of PPI interface mutation with drug response using linear model. All statistical analyses were performed using the R package (v4.2.0, http://www.r-project.org/).

System structural construction of EGFR-RAS-RAF-MEK-ERK signaling network.

EGR-EGFR complex were constructed by three crystal structures (PDB: 3NJP, 2M20, 2GS6). Membrane models were built by CHARMM-GUI (Wu et al., 2014). SOS1-KRAS complex (PDB: 6EPO), KRAS-RAF1 complex (PDB: 6VJJ), MEK1-BRAF complex (PDB: 6Q0J), MEK1 (PDB: 3WIG), and ERK1 (PDB: 4QTB) were accessed from the RCSB PDB protein data bank. Two subunits of RAF proteins are represented by RAF1 and BRAF, separately. The ITCH-BRAF complex model was generated using HADDOCK. All images were processed using PyMOL. The complex names, mutations and PDB ID were also shown in Table S10.

Cell viability assay

H1975 cells were transfected with NRF2 T80K/WT-expressing vectors or empty vectors using Lipofectamine 3000 (Thermofisher). For growth curve measurement, 3,000 cells were planted into 96-well plates, and viability was measured using CellTiter 96 AQueous MTS Reagent (Promega,) at days 0, 2 and 4.

Colony formation assay

For the colony formation assay, 2,000 cells were plated into 6-well plates. After 2 weeks, cells were fixed with 4% paraformaldehyde and stained with crystal violet. Relative growth index was analyzed using ImageJ software.

Web server development

The PIONEER web server is written in Python using the Django framework. The web server displays the full human interactome using co-crystal structures from PDB, homology models from Interactome3D (Mosca et al., 2013), and PIONEER-predicted interfaces. These data, along with auxiliary data about each protein, are stored on a Postgres database. The front-end displays this data using jQuery in two different web pages. The first page displays all information associated with a single protein-protein interaction. We display the protein-protein interaction interface information, show where the interface residues lie on the PFAM domains for each protein, and depict where the disease mutations are enriched on the interaction interface. The disease mutation information is obtained from HGMD. We display a number of 3D structures to help visualize the interaction interface. These includes the high-quality 3D structures from PDB and ModBase associated with each protein as well as any available high-quality PDB co-crystal structures. Furthermore, we display all AlphaFold structures associated with each protein. These structures are displayed using the MichelaNGLo viewer (Ferla et al., 2020). The second webpage displays a subset of the human interactome associated with a particular protein or a particular disease, depending on the user's input on the homepage. We use the springy.js network visualization library here.

The web server also hosts interaction data for eight species: *H. sapiens, A. thaliana, S. cerevisiae, D. melanogaster, C. elegans, M. musculus, S. pombe and E. coli*. Most importantly, the PIONEER web server also consists of an on-demand prediction

pipeline that allows users to predict the interaction interface between any two proteins given their UniProt IDs. The on-demand prediction pipeline returns the raw predictions made by PIONEER and shows the two-dimensional protein structure visualizing which regions of the protein are more likely to lie on the interaction interface. The prediction pipeline utilizes the SLURM job scheduler to serve these requests.

REFERENCES

1. Abi-Habib, R.J., Urieto, J.O., Liu, S., Leppla, S.H., Duesbery, N.S., and Frankel, A.E. (2005). BRAF status and mitogen-activated protein/extracellular signal-regulated kinase kinase 1/2 activity indicate sensitivity of melanoma cells to anthrax lethal toxin. Mol Cancer Ther *4*, 1303-1310.

2. Afsar Minhas, F.u.A., Geiss, B.J., and Ben-Hur, A. (2014). PAIRpred: Partner-specific prediction of interacting residues from sequence and structure. Proteins *82*, 1142-1155.

3. Altschul, S.F., Gish, W., Miller, W., Myers, E.W., and Lipman, D.J. (1990). Basic local alignment search tool. J Mol Biol *215*, 403-410.

4. Auton, A., Abecasis, G.R., Altshuler, D.M., Durbin, R.M., Abecasis, G.R., Bentley, D.R., Chakravarti, A., Clark, A.G., Donnelly, P., Eichler, E.E.*, et al.* (2015). A global reference for human genetic variation. Nature *526*, 68-74.

5. Baek, M., DiMaio, F., Anishchenko, I., Dauparas, J., Ovchinnikov, S., Lee, G.R., Wang, J., Cong, Q., Kinch, L.N., Schaeffer, R.D.*, et al.* (2021). Accurate prediction of protein structures and interactions using a three-track neural network. Science *373*, 871-876.

6. Barabási, A.-L., Gulbahce, N., and Loscalzo, J. (2011). Network medicine: a network-based approach to human disease. Nat Rev Genet *12*, 56-68.

7. Benjamini, Y., and Hochberg, Y. (1995). Controlling the False Discovery Rate: A Practical and Powerful Approach to Multiple Testing. J R Stat Soc Ser B Methodol *57*, 289-300.

8. Bianchi, F.M., Grattarola, D., Livi, L., and Alippi, C. (2022). Graph Neural Networks With Convolutional ARMA Filters. IEEE Trans Pattern Anal Mach Intell *44*, 3496-3507.

9. Bishayee, A., Beguinot, L., and Bishayee, S. (1999). Phosphorylation of Tyrosine 992, 1068, and 1086 Is Required for Conformational Change of the Human Epidermal Growth Factor Receptor C-Terminal Tail. Molecular Biology of the Cell *10*, 525-536.

10. Braberg, H., Echeverria, I., Kaake, R.M., Sali, A., and Krogan, N.J. (2022). From systems to structure - using genetic data to model protein structures. Nat Rev Genet *23*, 342-354.

11. Burke, D.F., Bryant, P., Barrio-Hernandez, I., Memon, D., Pozzati, G., Shenoy, A., Zhu, W., Dunham, A.S., Albanese, P., Keller, A.*, et al.* (2023). Towards a structurally resolved human protein interaction network. Nat Struct Mol Biol *30*, 216-225.

12. Burley, S.K., Bhikadiya, C., Bi, C., Bittrich, S., Chen, L., Crichlow, G.V., Duarte, J.M., Dutta, S., Fayazi, M., Feng, Z.*, et al.* (2022). RCSB Protein Data Bank: Celebrating 50 years of the PDB with new tools for understanding and visualizing biological macromolecules in 3D. Protein Sci *31*, 187-208.

13. Caunt, C.J., Sale, M.J., Smith, P.D., and Cook, S.J. (2015). MEK1 and MEK2 inhibitors and cancer therapy: the long and winding road. Nat Rev Cancer *15*, 577-592.

14. Chang, K., Creighton, C.J., Davis, C., Donehower, L., Drummond, J., Wheeler, D., Ally, A., Balasundaram, M., Birol, I., Butterfield, Y.S.N.*, et al.* (2013). The Cancer Genome Atlas Pan-Cancer analysis project. Nat Genet *45*, 1113-1120.

15. Cheng, F., Liang, H., Butte, A.J., Eng, C., and Nussinov, R. (2019). Personal Mutanomes Meet Modern Oncology Drug Discovery and Precision Health. Pharmacol Rev *71*, 1-19.

16. Cheng, F., Zhao, J., Wang, Y., Lu, W., Liu, Z., Zhou, Y., Martin, W.R., Wang, R., Huang, J., Hao, T.*, et al.* (2021). Comprehensive characterization of protein–protein interactions perturbed by disease mutations. Nat Genet *53*, 342-353.

17. Cho, K., van Merriënboer, B., Gulcehre, C., Bougares, F., Schwenk, H., and Bengio, Y. (2014). Learning Phrase Representations using RNN Encoder-Decoder for Statistical Machine Translation. Paper presented at: Empirical Methods in Natural Language Processing (Doha, Qatar).

18. Cho, M., Gong, J., Frankel, P., Synold, T.W., Lim, D., Chung, V., Chao, J., Li, D., Chen, Y., Sentovich, S.*, et al.* (2017). A phase I clinical trial of binimetinib in combination with FOLFOX in patients with advanced metastatic colorectal cancer who failed prior standard therapy. Oncotarget *8*, 79750-79760.

19. Chowdhury, R., Bouatta, N., Biswas, S., Floristean, C., Kharkar, A., Roy, K., Rochereau, C., Ahdritz, G., Zhang, J., Church, G.M.*, et al.* (2022). Single-sequence protein structure prediction using a language model and deep learning. Nat Biotechnol *40*, 1617-1623.

20. Corcoran, R.B., André, T., Atreya, C.E., Schellens, J.H.M., Yoshino, T., Bendell, J.C., Hollebecque, A., McRee, A.J., Siena, S., Middleton, G.*, et al.* (2018). Combined BRAF, EGFR, and MEK Inhibition in Patients with $BRAF^{V600E}$-Mutant Colorectal Cancer. Cancer Discov *8*, 428-443.

21. Cuadrado, A., Rojo, A.I., Wells, G., Hayes, J.D., Cousin, S.P., Rumsey, W.L., Attucks, O.C., Franklin, S., Levonen, A.-L., Kensler, T.W.*, et al.* (2019). Therapeutic targeting of the NRF2 and KEAP1 partnership in chronic diseases. Nat Rev Drug Discov *18*, 295-317.

22. Das, J., and Yu, H. (2012). HINT: High-quality protein interactomes and their applications in understanding human disease. BMC Syst Biol *6*, 92.

23. Dominguez, C., Boelens, R., and Bonvin, A.M.J.J. (2003). HADDOCK: A Protein−Protein Docking Approach Based on Biochemical or Biophysical Information. J Am Chem Soc *125*, 1731-1737.

24. Endres, N.F., Das, R., Smith, A.W., Arkhipov, A., Kovacs, E., Huang, Y., Pelton, J.G., Shan, Y., Shaw, D.E., Wemmer, D.E.*, et al.* (2013). Conformational coupling across the plasma membrane in activation of the EGF receptor. Cell *152*, 543-556.

25. Evans, R., O'Neill, M., Pritzel, A., Antropova, N., Senior, A., Green, T., Žídek, A., Bates, R., Blackwell, S., Yim, J.*, et al.* (2022). Protein complex prediction with AlphaFold-Multimer. bioRxiv, 2021.2010.2004.463034.

26. Favretto, F., Baker, J.D., Strohäker, T., Andreas, L.B., Blair, L.J., Becker, S., and Zweckstetter, M. (2020). The Molecular Basis of the Interaction of Cyclophilin A with α-Synuclein. Angew Chem Int Ed *59*, 5643-5646.

27. Ferla, M.P., Pagnamenta, A.T., Damerell, D., Taylor, J.C., and Marsden, B.D. (2020). MichelaNglo: sculpting protein views on web pages without coding. Bioinformatics *36*, 3268-3270.

28. Fout, A., Byrd, J., Shariat, B., and Ben-Hur, A. (2017). Protein interface prediction using graph convolutional networks. Paper presented at: Adv Neural Inf Process Syst (Long Beach, CA, USA).

29. Fu, L., Niu, B., Zhu, Z., Wu, S., and Li, W. (2012). CD-HIT: accelerated for clustering the next-generation sequencing data. Bioinformatics *28*, 3150-3152.

30. Fu, W., O'Connor, T.D., Jun, G., Kang, H.M., Abecasis, G., Leal, S.M., Gabriel, S., Rieder, M.J., Altshuler, D., Shendure, J.*, et al.* (2013). Analysis of 6,515 exomes reveals the recent origin of most human protein-coding variants. Nature *493*, 216-220.

31. Fukutomi, T., Takagi, K., Mizushima, T., Ohuchi, N., and Yamamoto, M. (2014). Kinetic, thermodynamic, and structural characterizations of the association between Nrf2-DLGex degron and Keap1. Mol Cell Biol *34*, 832-846.

32. Furukawa, M., and Xiong, Y. (2005). BTB protein Keap1 targets antioxidant transcription factor Nrf2 for ubiquitination by the Cullin 3-Roc1 ligase. Mol Cell Biol *25*, 162-171.

33. Gao, H., Korn, J.M., Ferretti, S., Monahan, J.E., Wang, Y., Singh, M., Zhang, C., Schnell, C., Yang, G., Zhang, Y.*, et al.* (2015). High-throughput screening using patient-derived tumor xenografts to predict clinical trial drug response. Nat Med *21*, 1318-1325.

34. Gary, W.B., Bis, J.C., Martin, E.R., Choi, S.H., DeStefano, A.L., Duijn, C.M.v., Fornage, M., Gabriel, S.B., Koboldt, D.C., Larson, D.E.*, et al.* (2017). The Alzheimer's Disease Sequencing Project: Study design and sample selection. Neurol Genet *3*, e194.

35. Glaser, F., Steinberg, D.M., Vakser, I.A., and Ben-Tal, N. (2001). Residue frequencies and pairing preferences at protein–protein interfaces. Proteins *43*, 89-102.

36. Guharoy, M., and Chakrabarti, P. (2010). Conserved residue clusters at protein-protein interfaces and their use in binding site identification. BMC Bioinformatics *11*, 286.

37. Han, Y., Lee, H., Park, J.C., and Yi, G.S. (2012). E3Net: a system for exploring E3-mediated regulatory networks of cellular functions. Mol Cell Proteomics *11*, O111.014076.

38. Hernández-Muñoz, I., Lund, A.H., van der Stoop, P., Boutsma, E., Muijrers, I., Verhoeven, E., Nusinow, D.A., Panning, B., Marahrens, Y., and van Lohuizen, M. (2005).

Stable X chromosome inactivation involves the PRC1 Polycomb complex and requires histone MACROH2A1 and the CULLIN3/SPOP ubiquitin E3 ligase. Proc Natl Acad Sci USA *102*, 7635-7640.

39. Hillig, R.C., Sautier, B., Schroeder, J., Moosmayer, D., Hilpmann, A., Stegmann, C.M., Werbeck, N.D., Briem, H., Boemer, U., Weiske, J.*, et al.* (2019). Discovery of potent SOS1 inhibitors that block RAS activation via disruption of the RAS–SOS1 interaction. Proc Natl Acad Sci USA *116*, 2551-2560.

40. Hofmann, M.H., Gmachl, M., Ramharter, J., Savarese, F., Gerlach, D., Marszalek, J.R., Sanderson, M.P., Kessler, D., Trapani, F., Arnhof, H.*, et al.* (2021a). BI-3406, a Potent and Selective SOS1–KRAS Interaction Inhibitor, Is Effective in KRAS-Driven Cancers through Combined MEK Inhibition. Cancer Discov *11*, 142-157.

41. Hofmann, M.H., Lu, H., Duenzinger, U., Gerlach, D., Trapani, F., Machado, A.A., Daniele, J.R., Waizenegger, I., Gmachl, M., Rudolph, D.*, et al.* (2021b). Abstract CT210: Trial in Process: Phase 1 studies of BI 1701963, a SOS1::KRAS Inhibitor, in combination with MEK inhibitors, irreversible KRASG12C inhibitors or irinotecan. Cancer Res *81*, CT210-CT210.

42. Huang, K.L., Wu, Y., Primeau, T., Wang, Y.T., Gao, Y., McMichael, J.F., Scott, A.D., Cao, S., Wendl, M.C., Johnson, K.J.*, et al.* (2019). Regulated Phosphosignaling Associated with Breast Cancer Subtypes and Druggability. Mol Cell Proteomics *18*, 1630-1650.

43. Huijberts, S.C.F.A., van Geel, R.M.J.M., van Brummelen, E.M.J., Opdam, F.L., Marchetti, S., Steeghs, N., Pulleman, S., Thijssen, B., Rosing, H., Monkhorst, K.*, et al.* (2020). Phase I study of lapatinib plus trametinib in patients with KRAS-mutant colorectal, non-small cell lung, and pancreatic cancer. Cancer Chemother Pharmacol *85*, 917-930.

44. Jumper, J., Evans, R., Pritzel, A., Green, T., Figurnov, M., Ronneberger, O., Tunyasuvunakool, K., Bates, R., Žídek, A., Potapenko, A.*, et al.* (2021). Highly accurate protein structure prediction with AlphaFold. Nature *596*, 583-589.

45. Keshava Prasad, T.S., Goel, R., Kandasamy, K., Keerthikumar, S., Kumar, S., Mathivanan, S., Telikicherla, D., Raju, R., Shafreen, B., Venugopal, A.*, et al.* (2009). Human Protein Reference Database—2009 update. Nucleic Acids Res *37*, D767-D772.

46. Kircher, M., Witten, D.M., Jain, P., O'Roak, B.J., Cooper, G.M., and Shendure, J. (2014). A general framework for estimating the relative pathogenicity of human genetic variants. Nat Genet *46*, 310-315.

47. Landrum, M.J., Lee, J.M., Benson, M., Brown, G., Chao, C., Chitipiralla, S., Gu, B., Hart, J., Hoffman, D., Hoover, J.*, et al.* (2016). ClinVar: public archive of interpretations of clinically relevant variants. Nucleic Acids Res *44*, D862-D868.

48. Lee, B., and Richards, F.M. (1971). The interpretation of protein structures: Estimation of static accessibility. J Mol Biol *55*, 379-IN374.

49. Lee, D., Xiong, D., Wierbowski, S., Li, L., Liang, S., and Yu, H. (2022). Deep learning methods for 3D structural proteome and interactome modeling. Curr Opin Struct Biol *73*, 102329.

50. Lek, M., Karczewski, K.J., Minikel, E.V., Samocha, K.E., Banks, E., Fennell, T., O'Donnell-Luria, A.H., Ware, J.S., Hill, A.J., Cummings, B.B.*, et al.* (2016). Analysis of protein-coding genetic variation in 60,706 humans. Nature *536*, 285-291.

51. Li, L., Xin, H., Xu, X., Huang, M., Zhang, X., Chen, Y., Zhang, S., Fu, X.Y., and Chang, Z. (2004). CHIP mediates degradation of Smad proteins and potentially regulates Smad-induced transcription. Mol Cell Biol *24*, 856-864.

52. Li, Y., Golding, G.B., and Ilie, L. (2021a). DELPHI: accurate deep ensemble model for protein interaction sites prediction. Bioinformatics *37*, 896-904.

53. Li, Z., Chen, S., Jhong, J.-H., Pang, Y., Huang, K.-Y., Li, S., and Lee, T.-Y. (2021b). UbiNet 2.0: a verified, classified, annotated and updated database of E3 ubiquitin ligase–substrate interactions. Database *2021*.

54. Li, Z.-N., Zhao, L., Yu, L.-F., and Wei, M.-J. (2020). BRAF and KRAS mutations in metastatic colorectal cancer: future perspectives for personalized therapy. Gastroenterol Rep *8*, 192-205.

55. Liang, S.I., van Lengerich, B., Eichel, K., Cha, M., Patterson, D.M., Yoon, T.-Y., von Zastrow, M., Jura, N., and Gartner, Z.J. (2018). Phosphorylated EGFR Dimers Are Not Sufficient to Activate Ras. Cell Rep *22*, 2593-2600.

56. Licata, L., Briganti, L., Peluso, D., Perfetto, L., Iannuccelli, M., Galeota, E., Sacco, F., Palma, A., Nardozza, A.P., Santonico, E.*, et al.* (2012). MINT, the molecular interaction database: 2012 update. Nucleic Acids Res *40*, D857-D861.

57. Lin, Q., Zhang, H., Ding, H., Qian, J., Lizaso, A., Lin, J., Han-Zhang, H., Xiang, J., Li, Y., and Zhu, H. (2019). The association between BRAF mutation class and clinical features in BRAF-mutant Chinese non-small cell lung cancer patients. J Transl Med *17*, 298.

58. Liu, F., Yang, X., Geng, M., and Huang, M. (2018). Targeting ERK, an Achilles' Heel of the MAPK pathway, in cancer therapy. Acta Pharm Sin B *8*, 552-562.

59. Liu, Q., Tong, D., Liu, G., Yi, Y., Zhang, D., Zhang, J., Zhang, Y., Huang, Z., Li, Y., Chen, R.*, et al.* (2017). HIF2A germline–mutation-induced polycythemia in a patient with VHL-associated renal-cell carcinoma. Cancer Biol Ther *18*, 944-947.

60. Lu, C., Mi, L.Z., Grey, M.J., Zhu, J., Graef, E., Yokoyama, S., and Springer, T.A. (2010). Structural evidence for loose linkage between ligand binding and kinase activation in the epidermal growth factor receptor. Mol Cell Biol *30*, 5432-5443.

61. Lv, D., Li, Y., Zhang, W., Alvarez, A.A., Song, L., Tang, J., Gao, W.-Q., Hu, B., Cheng, S.-Y., and Feng, H. (2017). TRIM24 is an oncogenic transcriptional co-activator of STAT3 in glioblastoma. Nat Commun *8*, 1454.

62. McLaren, W., Gil, L., Hunt, S.E., Riat, H.S., Ritchie, G.R.S., Thormann, A., Flicek, P., and Cunningham, F. (2016). The Ensembl Variant Effect Predictor. Genome Biology *17*, 122.

63. Mena, E.L., Kjolby, R.A.S., Saxton, R.A., Werner, A., Lew, B.G., Boyle, J.M., Harland, R., and Rape, M. (2018). Dimerization quality control ensures neuronal development and survival. Science *362*, eaap8236.

64. Mészáros, B., Kumar, M., Gibson, T.J., Uyar, B., and Dosztányi, Z. (2017). Degrons in cancer. Sci Signal *10*, eaak9982.

65. Mewes, H.W., Ruepp, A., Theis, F., Rattei, T., Walter, M., Frishman, D., Suhre, K., Spannagl, M., Mayer, K.F.X., Stümpflen, V.*, et al.* (2011). MIPS: curated databases and comprehensive secondary data resources in 2010. Nucleic Acids Res *39*, D220-D224.

66. Meyer, M.J., Beltrán, J.F., Liang, S., Fragoza, R., Rumack, A., Liang, J., Wei, X., and Yu, H. (2018). Interactome INSIDER: a structural interactome browser for genomic studies. Nat Methods *15*, 107-114.

67. Mintseris, J., and Weng, Z. (2005). Structure, function, and evolution of transient and obligate protein–protein interactions. Proc Natl Acad Sci USA *102*, 10930-10935.

68. Mosca, R., Céol, A., and Aloy, P. (2013). Interactome3D: adding structural details to protein networks. Nat Methods *10*, 47-53.

69. Nguyen, B., Fong, C., Luthra, A., Smith, S.A., DiNatale, R.G., Nandakumar, S., Walch, H., Chatila, W.K., Madupuri, R., Kundra, R.*, et al.* (2022). Genomic characterization of metastatic patterns from prospective clinical sequencing of 25,000 patients. Cell *185*, 563-575.e511.

70. Nussinov, R., Jang, H., Nir, G., Tsai, C.J., and Cheng, F. (2022). Open Structural Data in Precision Medicine. Annu Rev Biomed Data Sci *5*, 95-117.

71. Orchard, S., Ammari, M., Aranda, B., Breuza, L., Briganti, L., Broackes-Carter, F., Campbell, N.H., Chavali, G., Chen, C., del-Toro, N.*, et al.* (2014). The MIntAct project—IntAct as a common curation platform for 11 molecular interaction databases. Nucleic Acids Res *42*, D358-D363.

72. Ostertag, M.S., Hutwelker, W., Plettenburg, O., Sattler, M., and Popowicz, G.M. (2019a). Structural Insights into BET Client Recognition of Endometrial and Prostate Cancer-Associated SPOP Mutants. J Mol Biol *431*, 2213-2221.

73. Ostertag, M.S., Messias, A.C., Sattler, M., and Popowicz, G.M. (2019b). The Structure of the SPOP-Pdx1 Interface Reveals Insights into the Phosphorylation-Dependent Binding Regulation. Structure *27*, 327-334.e323.

74. Oughtred, R., Stark, C., Breitkreutz, B.-J., Rust, J., Boucher, L., Chang, C., Kolas, N., O'Donnell, L., Leung, G., McAdam, R.*, et al.* (2019). The BioGRID interaction database: 2019 update. Nucleic Acids Res *47*, D529-D541.

75. Patelli, G., Tosi, F., Amatu, A., Mauri, G., Curaba, A., Patanè, D.A., Pani, A., Scaglione, F., Siena, S., and Sartore-Bianchi, A. (2021). Strategies to tackle RAS-mutated metastatic colorectal cancer. ESMO Open *6*, 100156.

76. Pieper, U., Webb, B.M., Dong, G.Q., Schneidman-Duhovny, D., Fan, H., Kim, S.J., Khuri, N., Spill, Y.G., Weinkam, P., Hammel, M.*, et al.* (2014). ModBase, a database of annotated comparative protein structure models and associated resources. Nucleic Acids Res *42*, D336-D346.

77. Pierce, B.G., Wiehe, K., Hwang, H., Kim, B.-H., Vreven, T., and Weng, Z. (2014). ZDOCK server: interactive docking prediction of protein–protein complexes and symmetric multimers. Bioinformatics *30*, 1771-1773.

78. Plasilova, M., Chattopadhyay, C., Pal, P., Schaub, N.A., Buechner, S.A., Mueller, H., Miny, P., Ghosh, A., and Heinimann, K. (2004). Homozygous missense mutation in the lamin A/C gene causes autosomal recessive Hutchinson-Gilford progeria syndrome. J Med Genet *41*, 609.

79. Rabara, D., Tran, T.H., Dharmaiah, S., Stephens, R.M., McCormick, F., Simanshu, D.K., and Holderfield, M. (2019). KRAS G13D sensitivity to neurofibromin-mediated GTP hydrolysis. Proc Natl Acad Sci USA *116*, 22122-22131.

80. Roberts, P.J., and Der, C.J. (2007). Targeting the Raf-MEK-ERK mitogen-activated protein kinase cascade for the treatment of cancer. Oncogene *26*, 3291-3310.

81. Sahni, N., Yi, S., Taipale, M., Fuxman Bass, Juan I., Coulombe-Huntington, J., Yang, F., Peng, J., Weile, J., Karras, Georgios I., Wang, Y.*, et al.* (2015). Widespread Macromolecular Interaction Perturbations in Human Genetic Disorders. Cell *161*, 647-660.

82. Salwinski, L., Miller, C.S., Smith, A.J., Pettit, F.K., Bowie, J.U., and Eisenberg, D. (2004). The Database of Interacting Proteins: 2004 update. Nucleic Acids Res *32*, D449-D451.

83. Sanchez-Garcia, R., Macias, J.R., Sorzano, C.O.S., Carazo, J.M., and Segura, J. (2022). BIPSPI+: Mining Type-Specific Datasets of Protein Complexes to Improve Protein Binding Site Prediction. J Mol Biol *434*, 167556.

84. Sanchez-Garcia, R., Sorzano, C.O.S., Carazo, J.M., and Segura, J. (2019). BIPSPI: a method for the prediction of partner-specific protein–protein interfaces. Bioinformatics *35*, 470-477.

85. Scardapane, S., Van Vaerenbergh, S., Totaro, S., and Uncini, A. (2019). Kafnets: Kernel-based non-parametric activation functions for neural networks. Neural Netw *110*, 19-32.

86. Schneider, C.A., Rasband, W.S., and Eliceiri, K.W. (2012). NIH Image to ImageJ: 25 years of image analysis. Nat Methods *9*, 671-675.

87. Schymkowitz, J., Borg, J., Stricher, F., Nys, R., Rousseau, F., and Serrano, L. (2005). The FoldX web server: an online force field. Nucleic Acids Res *33*, W382-W388.

88. Senft, D., Qi, J., and Ronai, Z.e.A. (2018). Ubiquitin ligases in oncogenic transformation and cancer therapy. Nat Rev Cancer *18*, 69-88.

89. Shannon, P., Markiel, A., Ozier, O., Baliga, N.S., Wang, J.T., Ramage, D., Amin, N., Schwikowski, B., and Ideker, T. (2003). Cytoscape: A Software Environment for Integrated Models of Biomolecular Interaction Networks. Genome Res *13*, 2498-2504.

90. Siegelin, M.D., and Borczuk, A.C. (2014). Epidermal growth factor receptor mutations in lung adenocarcinoma. Lab Invest *94*, 129-137.

91. Sievers, F., and Higgins, D.G. (2018). Clustal Omega for making accurate alignments of many protein sequences. Protein Sci *27*, 135-145.

92. Song, Y., Xu, Y., Pan, C., Yan, L., Wang, Z.-w., and Zhu, X. (2020). The emerging role of SPOP protein in tumorigenesis and cancer therapy. Mol Cancer *19*, 2.

93. Stenson, P.D., Mort, M., Ball, E.V., Evans, K., Hayden, M., Heywood, S., Hussain, M., Phillips, A.D., and Cooper, D.N. (2017). The Human Gene Mutation Database: towards a comprehensive repository of inherited mutation data for medical research, genetic diagnosis and next-generation sequencing studies. Hum Genet *136*, 665-677.

94. Taliun, D., Harris, D.N., Kessler, M.D., Carlson, J., Szpiech, Z.A., Torres, R., Taliun, S.A.G., Corvelo, A., Gogarten, S.M., Kang, H.M.*, et al.* (2021). Sequencing of 53,831 diverse genomes from the NHLBI TOPMed Program. Nature *590*, 290-299.

95. Tarade, D., Robinson, C.M., Lee, J.E., and Ohh, M. (2018). HIF-2α-pVHL complex reveals broad genotype-phenotype correlations in HIF-2α-driven disease. Nat Commun *9*, 3359.

96. Townshend, R., Bedi, R., Suriana, P., and Dror, R. (2019). End-to-end learning on 3D protein structure for interface prediction. Paper presented at: Adv Neural Inf Process Syst (Vancouver, Canada).

97. Tran, T.H., Chan, A.H., Young, L.C., Bindu, L., Neale, C., Messing, S., Dharmaiah, S., Taylor, T., Denson, J.-P., Esposito, D.*, et al.* (2021). KRAS interaction with RAF1 RAS-binding domain and cysteine-rich domain provides insights into RAS-mediated RAF activation. Nat Commun *12*, 1176.

98. Tsai, W.-W., Wang, Z., Yiu, T.T., Akdemir, K.C., Xia, W., Winter, S., Tsai, C.-Y., Shi, X., Schwarzer, D., Plunkett, W.*, et al.* (2010). TRIM24 links a non-canonical histone signature to breast cancer. Nature *468*, 927-932.

99. Tubiana, J., Schneidman-Duhovny, D., and Wolfson, H.J. (2022). ScanNet: an interpretable geometric deep learning model for structure-based protein binding site prediction. Nat Methods *19*, 730-739.

100. Turner, B., Razick, S., Turinsky, A.L., Vlasblom, J., Crowdy, E.K., Cho, E., Morrison, K., Donaldson, I.M., and Wodak, S.J. (2010). iRefWeb: interactive analysis of consolidated protein interaction data and their supporting evidence. Database *2010*, baq023.

101. V, F.R.L., Zhuang, Z., Yang, C., Fui, M.N.T., Vankayalapati, H., Pacak, K., and Prchal, J.T. (2012). Three Novel EPAS1/HIF2A Somatic and Germline mutations Associated with Polycythemia and Pheochromocytoma/Paraganglioma. Blood *120*, 2080-2080.

102. Vasaikar, S., Huang, C., Wang, X., Petyuk, V.A., Savage, S.R., Wen, B., Dou, Y., Zhang, Y., Shi, Z., Arshad, O.A.*, et al.* (2019). Proteogenomic Analysis of Human Colon Cancer Reveals New Therapeutic Opportunities. Cell *177*, 1035-1049.e1019.

103. Velankar, S., Dana, J.M., Jacobsen, J., van Ginkel, G., Gane, P.J., Luo, J., Oldfield, T.J., O'Donovan, C., Martin, M.-J., and Kleywegt, G.J. (2013). SIFTS: Structure Integration with Function, Taxonomy and Sequences resource. Nucleic Acids Res *41*, D483-D489.

104. Vidal, M., Cusick, Michael E., and Barabási, A.-L. (2011). Interactome Networks and Human Disease. Cell *144*, 986-998.

105. Walhout, A.J.M., and Vidal, M. (2001). High-Throughput Yeast Two-Hybrid Assays for Large-Scale Protein Interaction Mapping. Methods *24*, 297-306.

106. Wang, D., Ma, J., Botuyan, M.V., Cui, G., Yan, Y., Ding, D., Zhou, Y., Krueger, E.W., Pei, J., Wu, X.*, et al.* (2021). ATM-phosphorylated SPOP contributes to 53BP1 exclusion from chromatin during DNA replication. Sci Adv *7*.

107. Wang, Q., Moyret-Lalle, C., Couzon, F., Surbiguet-Clippe, C., Saurin, J.C., Lorca, T., Navarro, C., and Puisieux, A. (2003). Alterations of anaphase-promoting complex genes in human colon cancer cells. Oncogene *22*, 1486-1490.

108. Wang, S., Li, W., Liu, S., and Xu, J. (2016). RaptorX-Property: a web server for protein structure property prediction. Nucleic Acids Res *44*, W430-W435.

109. Wang, X., Wei, X., Thijssen, B., Das, J., Lipkin, S.M., and Yu, H. (2012). Three-dimensional reconstruction of protein networks provides insight into human genetic disease. Nat Biotechnol *30*, 159-164.

110. Wang, Z., Song, Y., Ye, M., Dai, X., Zhu, X., and Wei, W. (2020). The diverse roles of SPOP in prostate cancer and kidney cancer. Nat Rev Urol *17*, 339-350.

111. Wei, X., Das, J., Fragoza, R., Liang, J., Bastos de Oliveira, F.M., Lee, H.R., Wang, X., Mort, M., Stenson, P.D., Cooper, D.N.*, et al.* (2014). A Massively Parallel Pipeline to Clone DNA Variants and Examine Molecular Phenotypes of Human Disease Mutations. PLoS Genet *10*, e1004819.

112. Wierbowski, S.D., Liang, S., Liu, Y., Chen, Y., Gupta, S., Andre, N.M., Lipkin, S.M., Whittaker, G.R., and Yu, H. (2021). A 3D structural SARS-CoV-2-human interactome to explore genetic and drug perturbations. Nat Methods *18*, 1477-1488.

113. Wu, E.L., Cheng, X., Jo, S., Rui, H., Song, K.C., Dávila-Contreras, E.M., Qi, Y., Lee, J., Monje-Galvan, V., Venable, R.M.*, et al.* (2014). CHARMM-GUI Membrane Builder toward realistic biological membrane simulations. J Comput Chem *35*, 1997-2004.

114. Xiong, D., Lee, D., Li, L., Zhao, Q., and Yu, H. (2022). Implications of disease-related mutations at protein–protein interfaces. Curr Opin Struct Biol *72*, 219-225.

115. Xu, J., and Lin, D.I. (2018). Oncogenic c-terminal cyclin D1 (CCND1) mutations are enriched in endometrioid endometrial adenocarcinomas. PLoS One *13*, e0199688.

116. Xue, L.C., Dobbs, D., Bonvin, A.M.J.J., and Honavar, V. (2015). Computational prediction of protein interfaces: A review of data driven methods. FEBS Lett *589*, 3516-3526.

117. Yang, Q., Zhao, J., Chen, D., and Wang, Y. (2021). E3 ubiquitin ligases: styles, structures and functions. Mol Biomed *2*, 23.

118. Yin, Q., Wyatt, C.J., Han, T., Smalley, K.S.M., and Wan, L. (2020). ITCH as a potential therapeutic target in human cancers. Semin Cancer Biol *67*, 117-130.

119. You, X., Kong, G., Ranheim, E.A., Yang, D., Zhou, Y., and Zhang, J. (2018). Unique dependence on Sos1 in Kras (G12D) -induced leukemogenesis. Blood *132*, 2575-2579.

120. Zeng, M., Zhang, F., Wu, F.-X., Li, Y., Wang, J., and Li, M. (2020). Protein-protein interaction site prediction through combining local and global features with deep neural networks. Bioinformatics *36*, 1114-1120.

121. Zhang, B., Li, J., Quan, L., Chen, Y., and Lü, Q. (2019). Sequence-based prediction of protein-protein interaction sites by simplified long short-term memory network. Neurocomputing *357*, 86-100.

122. Zhang, J., and Kurgan, L. (2019). SCRIBER: accurate and partner type-specific prediction of protein-binding residues from proteins sequences. Bioinformatics *35*, i343-i353.

123. Zhou, Y., Hou, Y., Shen, J., Mehra, R., Kallianpur, A., Culver, D.A., Gack, M.U., Farha, S., Zein, J., Comhair, S.*, et al.* (2020). A network medicine approach to investigation and population-based validation of disease manifestations and drug repurposing for COVID-19. PLoS Biol *18*, e3000970.

124. Zhuang, F., Qi, Z., Duan, K., Xi, D., Zhu, Y., Zhu, H., Xiong, H., and He, Q. (2021). A Comprehensive Survey on Transfer Learning. Proc IEEE *109*, 43-76.

Figure 1

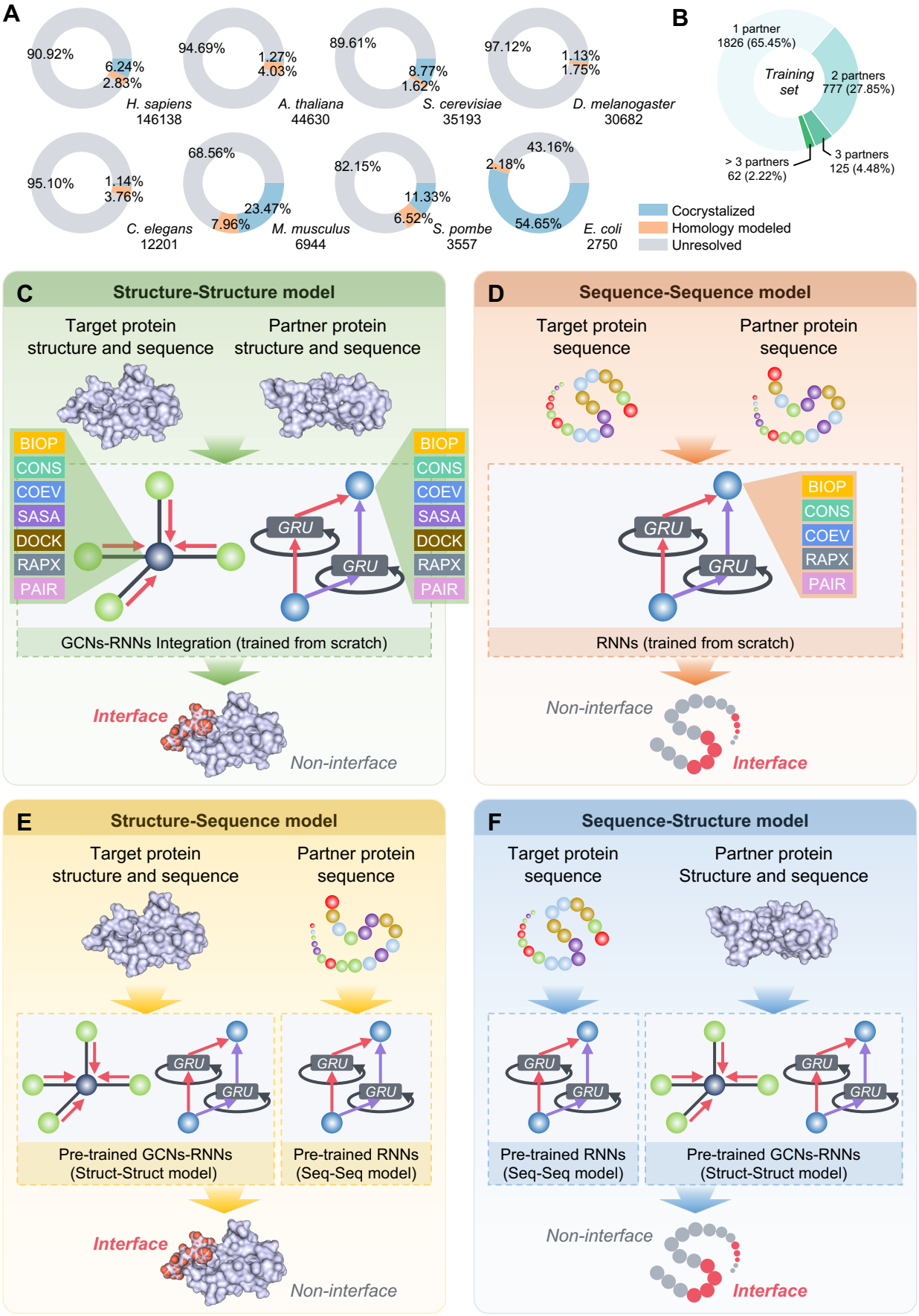
A
90.92%
6.24%
2.83%
H. sapiens
146138
94.69%
1.27%
4.03%
A. thaliana
44630
89.61%
8.77%
1.62%
S. cerevisiae
35193
97.12%
1.13%
1.75%
D. melanogaster
30682
95.10%
1.14%
3.76%
C. elegans
12201
68.56%
23.47%
7.96%
M. musculus
6944
82.15%
11.33%
6.52%
S. pombe
3557
43.16%
2.18%
54.65%
E. coli
2750
Cocrystalized
Homology modeled
Unresolved
B
1 partner
1826 (65.45%)
Training set
2 partners
777 (27.85%)
3 partners
125 (4.48%)
> 3 partners
62 (2.22%)
C
Structure-Structure model
Target protein structure and sequence
Partner protein structure and sequence
BIOP
CONS
COEV
SASA
DOCK
RAPX
PAIR
GRU
GCNs-RNNs Integration (trained from scratch)
Interface
Non-interface
D
Sequence-Sequence model
Target protein sequence
Partner protein sequence
RNNs (trained from scratch)
Non-interface
Interface
E
Structure-Sequence model
Target protein structure and sequence
Partner protein sequence
Pre-trained GCNs-RNNs (Struct-Struct model)
Pre-trained RNNs (Seq-Seq model)
Interface
Non-interface
F
Sequence-Structure model
Target protein sequence
Partner protein Structure and sequence
Pre-trained RNNs (Seq-Seq model)
Pre-trained GCNs-RNNs (Struct-Struct model)
Non-interface
Interface

Figure 2

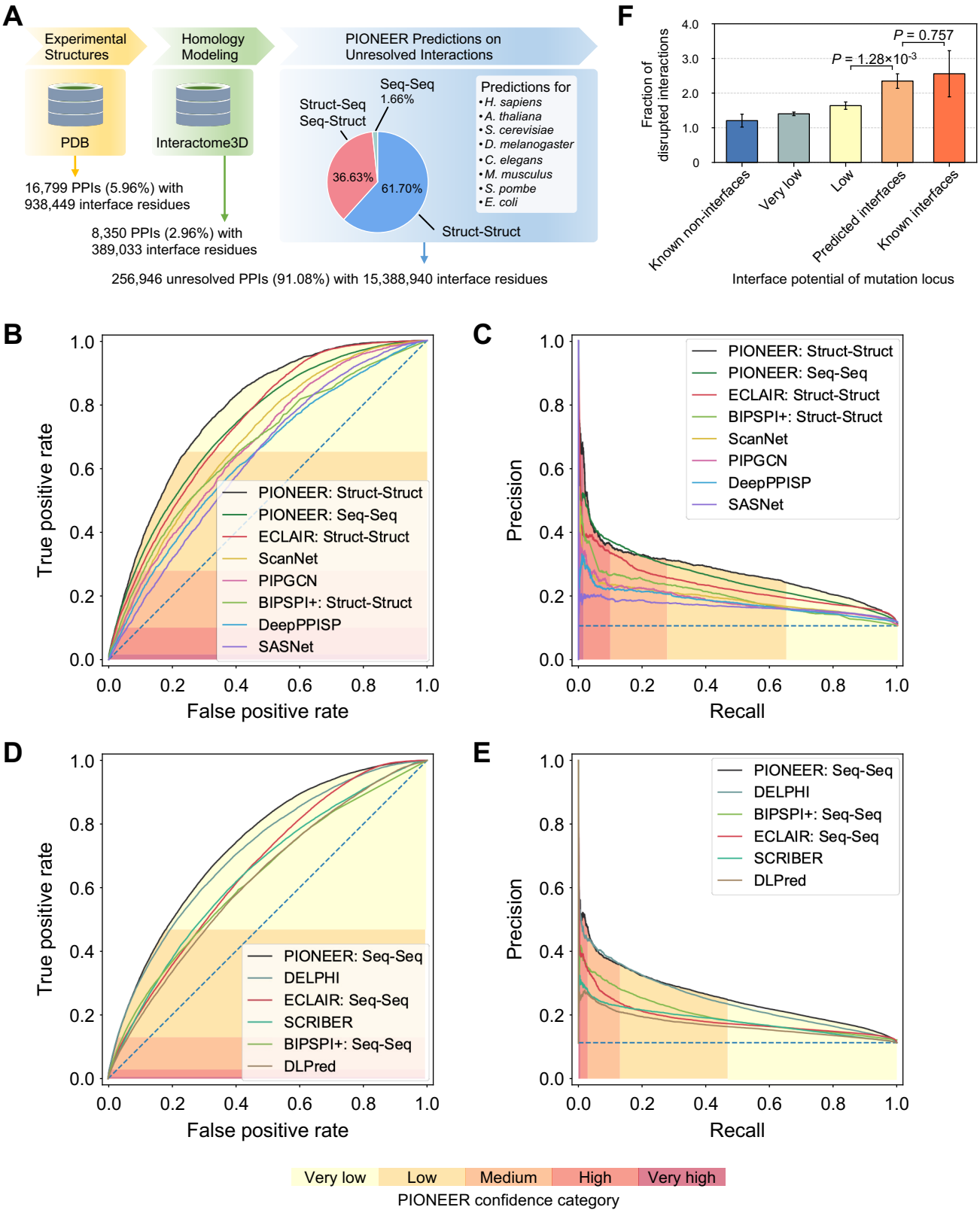
A
Experimental Structures
Homology Modeling
PIONEER Predictions on Unresolved Interactions
PDB
Interactome3D
16,799 PPIs (5.96%) with 938,449 interface residues
8,350 PPIs (2.96%) with 389,033 interface residues
Seq-Seq 1.66%
Struct-Seq Seq-Struct
36.63%
61.70%
Struct-Struct
Predictions for
• H. sapiens
• A. thaliana
• S. cerevisiae
• D. melanogaster
• C. elegans
• M. musculus
• S. pombe
• E. coli
256,946 unresolved PPIs (91.08%) with 15,388,940 interface residues
F
Fraction of disrupted interactions
P = 0.757
P = 1.28×10-3
Known non-interfaces
Very low
Low
Predicted interfaces
Known interfaces
Interface potential of mutation locus
B
True positive rate
False positive rate
PIONEER: Struct-Struct
PIONEER: Seq-Seq
ECLAIR: Struct-Struct
ScanNet
PIPGCN
BIPSPI+: Struct-Struct
DeepPPISP
SASNet
C
Precision
Recall
PIONEER: Struct-Struct
PIONEER: Seq-Seq
ECLAIR: Struct-Struct
BIPSPI+: Struct-Struct
ScanNet
PIPGCN
DeepPPISP
SASNet
D
True positive rate
False positive rate
PIONEER: Seq-Seq
DELPHI
ECLAIR: Seq-Seq
SCRIBER
BIPSPI+: Seq-Seq
DLPred
E
Precision
Recall
PIONEER: Seq-Seq
DELPHI
BIPSPI+: Seq-Seq
ECLAIR: Seq-Seq
SCRIBER
DLPred
Very low
Low
Medium
High
Very high
PIONEER confidence category

Figure 3

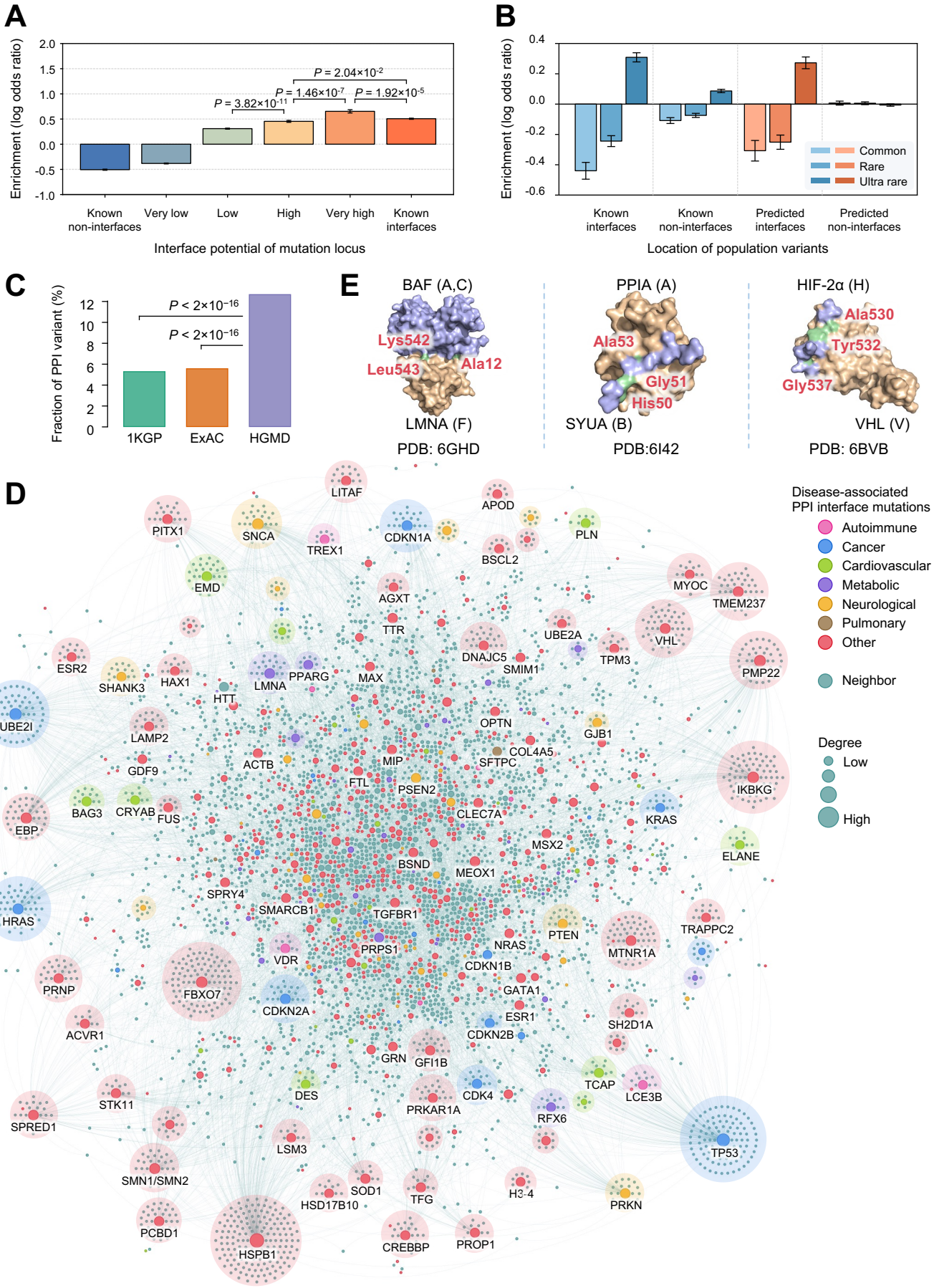
A
Enrichment (log odds ratio)
2.0
1.5
1.0
0.5
0.0
-0.5
-1.0
P = 3.82×10-11
P = 1.46×10-7
P = 1.92×10-5
P = 2.04×10-2
Known non-interfaces
Very low
Low
High
Very high
Known interfaces
Interface potential of mutation locus
B
Enrichment (log odds ratio)
0.4
0.2
0.0
-0.2
-0.4
-0.6
Common
Rare
Ultra rare
Known interfaces
Known non-interfaces
Predicted interfaces
Predicted non-interfaces
Location of population variants
C
Fraction of PPI variant (%)
12
10
8
6
4
2
0
P < 2×10−16
P < 2×10−16
1KGP
ExAC
HGMD
E
BAF (A,C)
Lys542
Leu543
Ala12
LMNA (F)
PDB: 6GHD
PPIA (A)
Ala53
Gly51
His50
SYUA (B)
PDB:6I42
HIF-2α (H)
Ala530
Tyr532
Gly537
VHL (V)
PDB: 6BVB
D
Disease-associated PPI interface mutations
Autoimmune
Cancer
Cardiovascular
Metabolic
Neurological
Pulmonary
Other
Neighbor
Degree
Low
High
LITAF
APOD
PITX1
SNCA
TREX1
CDKN1A
PLN
BSCL2
EMD
AGXT
MYOC
TMEM237
TTR
UBE2A
VHL
ESR2
SHANK3
HAX1
LMNA
PPARG
MAX
DNAJC5
SMIM1
TPM3
PMP22
HTT
UBE2I
LAMP2
OPTN
GJB1
COL4A5
GDF9
ACTB
MIP
SFTPC
FTL
PSEN2
IKBKG
BAG3
CRYAB
FUS
CLEC7A
KRAS
EBP
MSX2
ELANE
BSND
MEOX1
SPRY4
HRAS
SMARCB1
TGFBR1
PTEN
TRAPPC2
NRAS
MTNR1A
VDR
PRPS1
CDKN1B
PRNP
FBXO7
GATA1
CDKN2A
ESR1
SH2D1A
ACVR1
CDKN2B
GRN
GFI1B
TCAP
LCE3B
DES
CDK4
STK11
PRKAR1A
RFX6
SPRED1
LSM3
TP53
SMN1/SMN2
SOD1
TFG
H3-4
PRKN
HSD17B10
PCBD1
HSPB1
CREBBP
PROP1

Figure 4

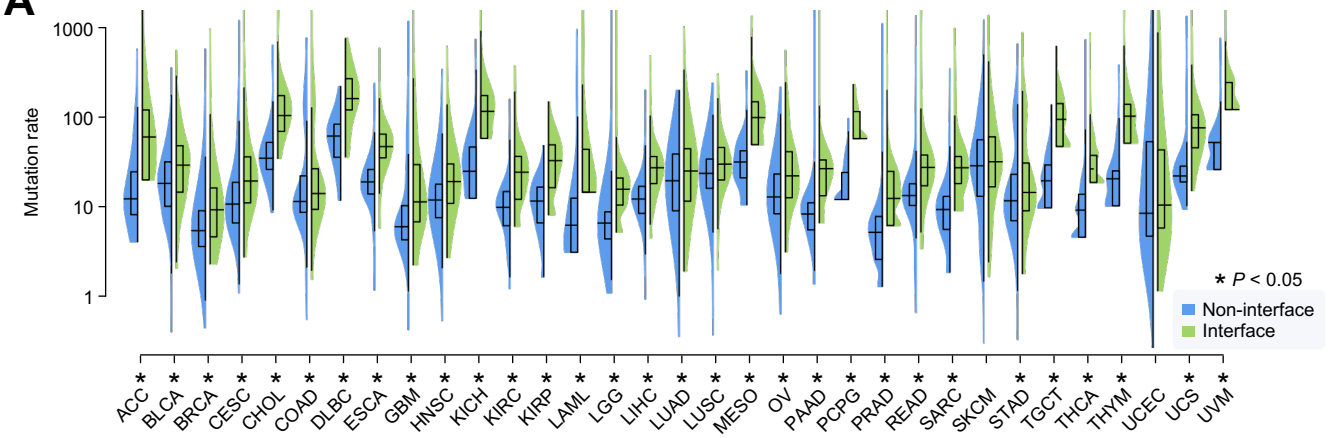
A
Mutation rate
1000
100
10
1
* P < 0.05
Non-interface
Interface
ACC
BLCA
BRCA
CESC
CHOL
COAD
DLBC
ESCA
GBM
HNSC
KICH
KIRC
KIRP
LAML
LGG
LIHC
LUAD
LUSC
MESO
OV
PAAD
PCPG
PRAD
READ
SARC
SKCM
STAD
TGCT
THCA
THYM
UCEC
UCS
UVM

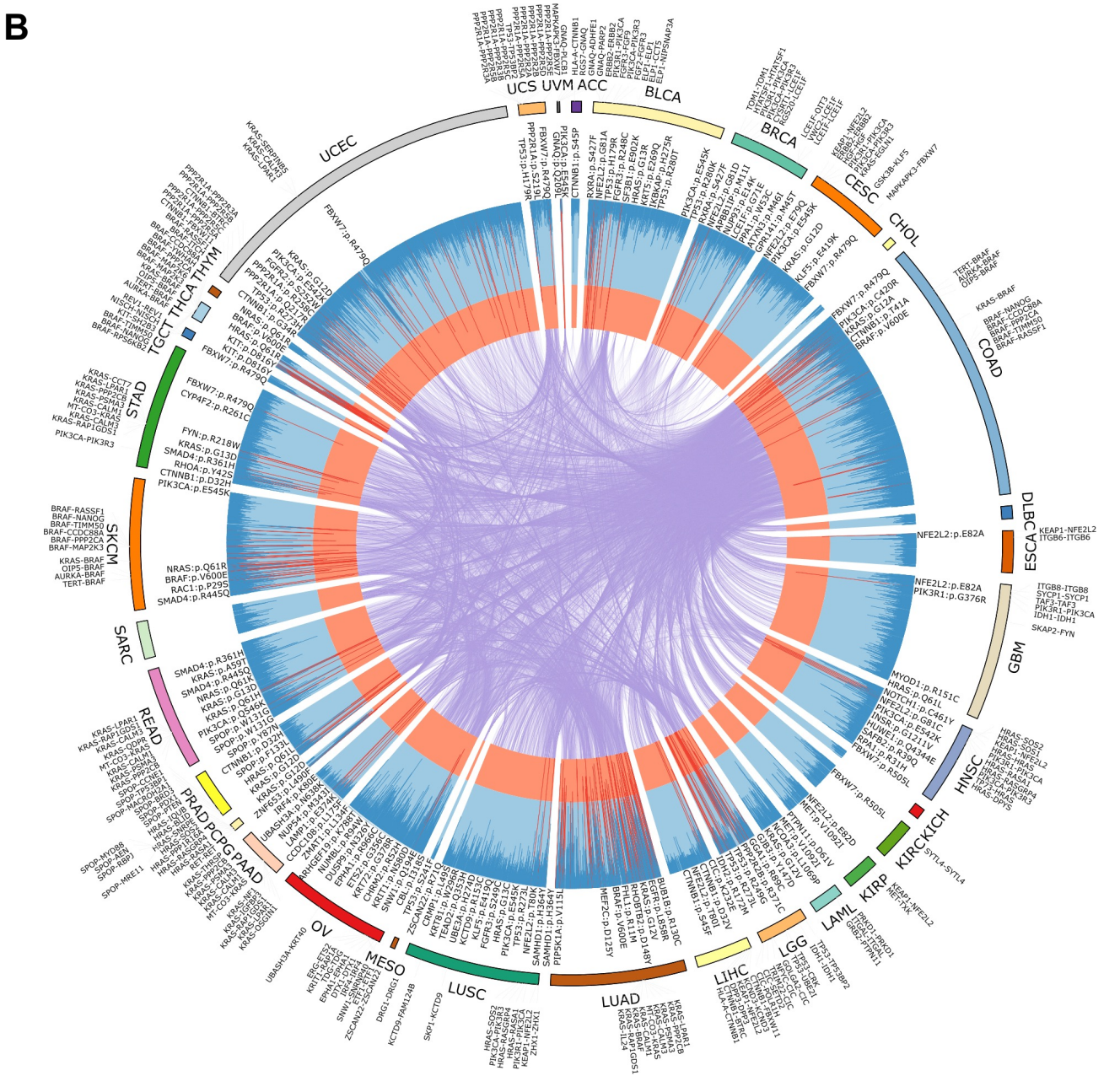
B
UCS UVM ACC
BLCA
BRCA
CESC
CHOL
COAD
DLBC
ESCA
GBM
HNSC
KIRCKICH
KIRP
LAML
LGG
LIHC
LUAD
LUSC
MESO
OV
PAAD
PCPG
PRAD
READ
SARC
SKCM
STAD
TGCT THCA THYM
UCEC

Figure 5

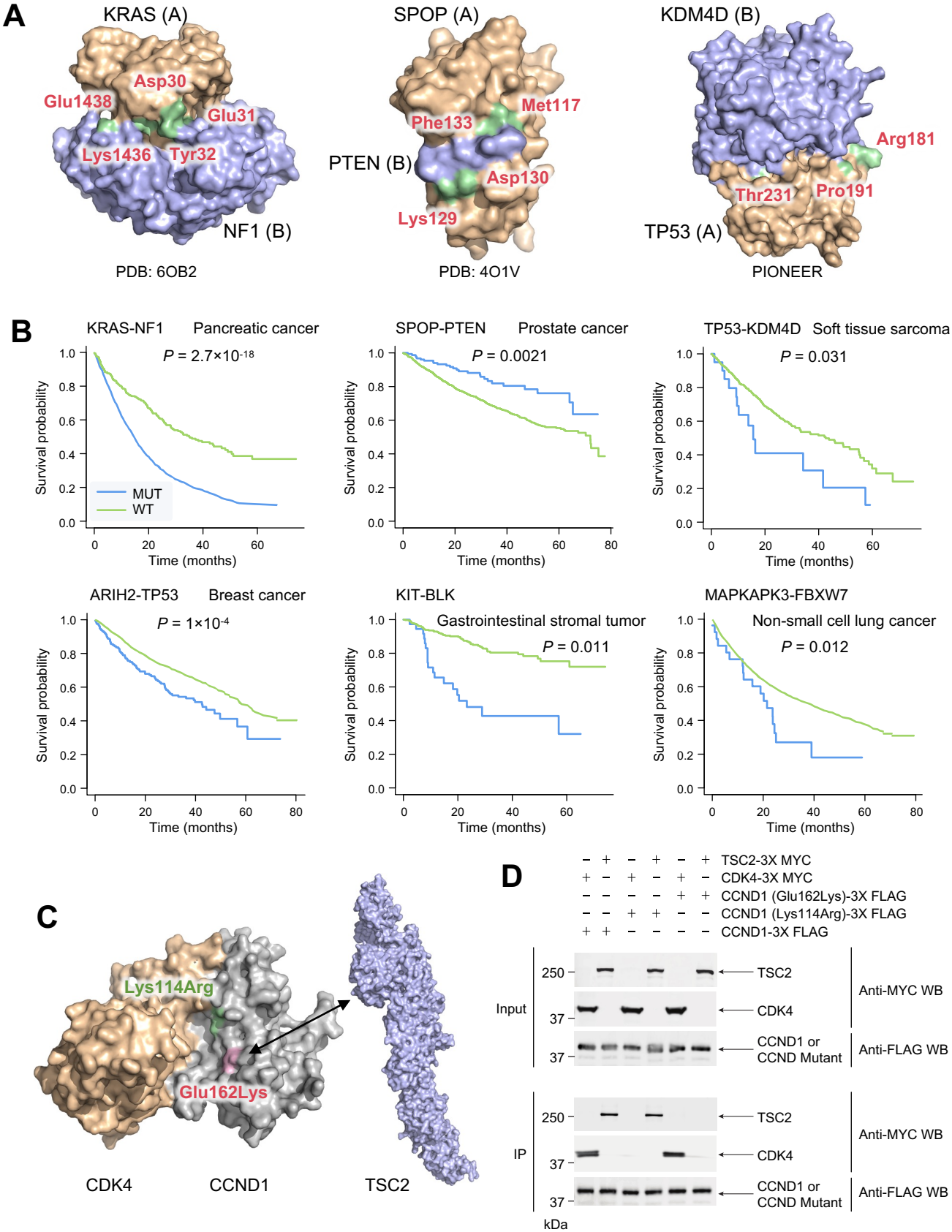
A
KRAS (A)
Asp30
Glu1438
Glu31
Lys1436
Tyr32
NF1 (B)
PDB: 6OB2
SPOP (A)
Met117
Phe133
PTEN (B)
Asp130
Lys129
PDB: 4O1V
KDM4D (B)
Arg181
Thr231
Pro191
TP53 (A)
PIONEER
B
KRAS-NF1 Pancreatic cancer
P = 2.7×10-18
MUT
WT
SPOP-PTEN Prostate cancer
P = 0.0021
TP53-KDM4D Soft tissue sarcoma
P = 0.031
ARIH2-TP53 Breast cancer
P = 1×10-4
KIT-BLK
Gastrointestinal stromal tumor
P = 0.011
MAPKAPK3-FBXW7
Non-small cell lung cancer
P = 0.012
Survival probability
Time (months)
C
Lys114Arg
Glu162Lys
CDK4
CCND1
TSC2
D
TSC2-3X MYC
CDK4-3X MYC
CCND1 (Glu162Lys)-3X FLAG
CCND1 (Lys114Arg)-3X FLAG
CCND1-3X FLAG
Input
IP
250
37
TSC2
CDK4
CCND1 or CCND Mutant
Anti-MYC WB
Anti-FLAG WB
kDa

Figure 6

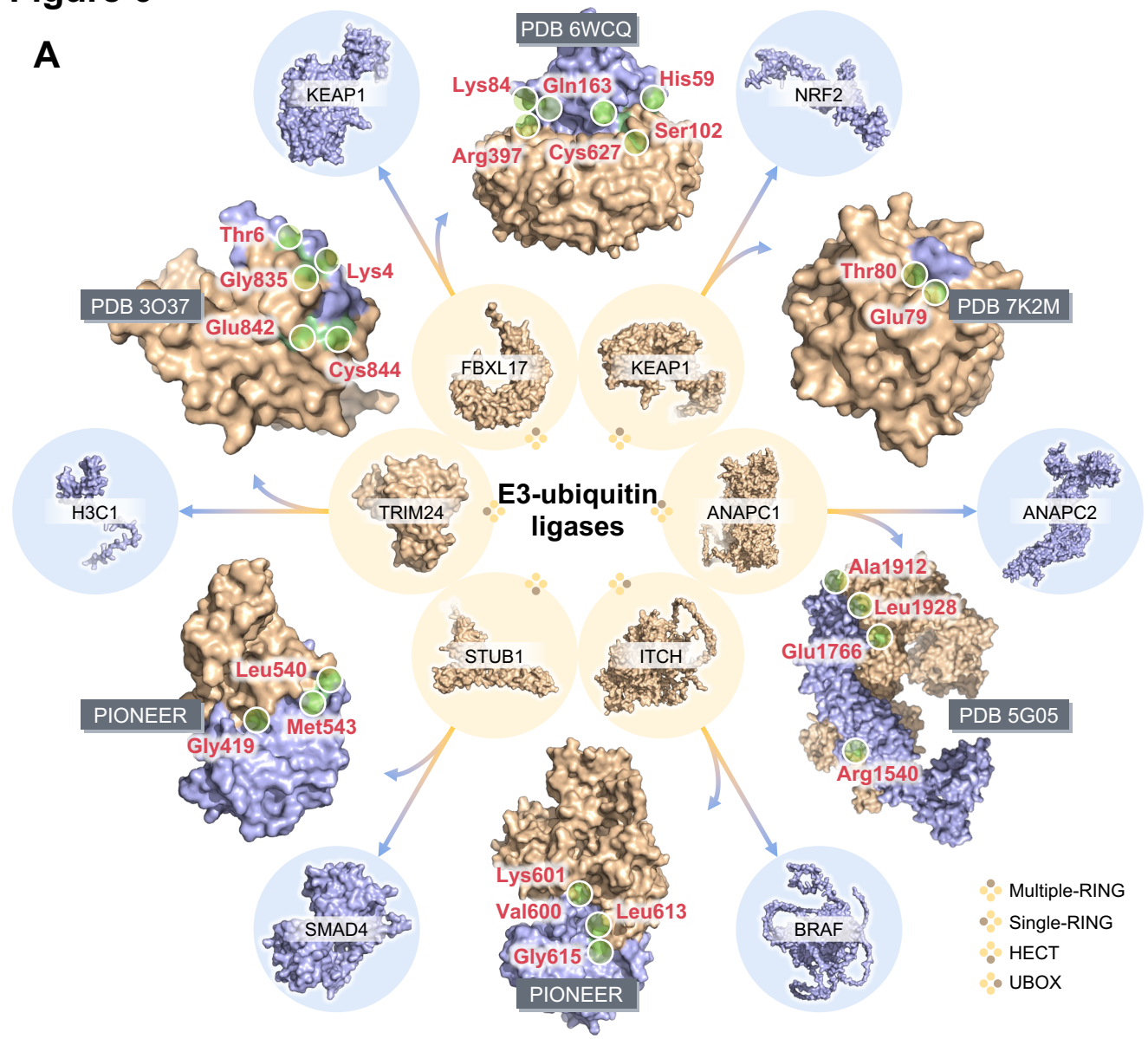
A
PDB 6WCQ
KEAP1
Lys84
Gln163
His59
Ser102
Arg397
Cys627
NRF2
Thr6
Lys4
Gly835
Glu842
Cys844
PDB 3O37
Thr80
Glu79
PDB 7K2M
FBXL17
KEAP1
H3C1
TRIM24
E3-ubiquitin ligases
ANAPC1
ANAPC2
Ala1912
Leu1928
Glu1766
Arg1540
PDB 5G05
STUB1
ITCH
Leu540
Met543
Gly419
PIONEER
SMAD4
Lys601
Val600
Leu613
Gly615
PIONEER
BRAF
Multiple-RING
Single-RING
HECT
UBOX

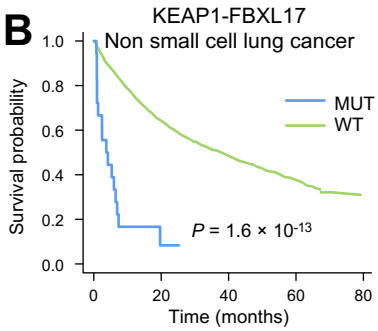
B
KEAP1-FBXL17
Non small cell lung cancer
Survival probability
MUT
WT
P = 1.6 × 10-13
Time (months)

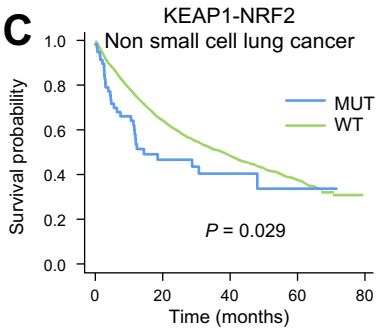
C
KEAP1-NRF2
Non small cell lung cancer
Survival probability
MUT
WT
P = 0.029
Time (months)

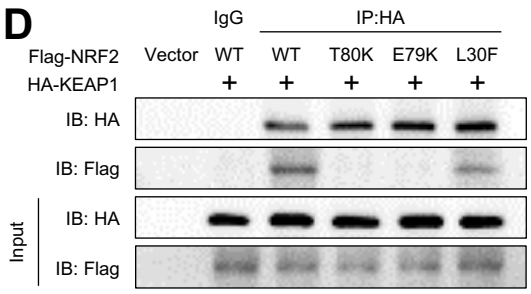
D
IgG
IP:HA
Flag-NRF2
Vector
WT
WT
T80K
E79K
L30F
HA-KEAP1
IB: HA
IB: Flag
Input
IB: HA
IB: Flag

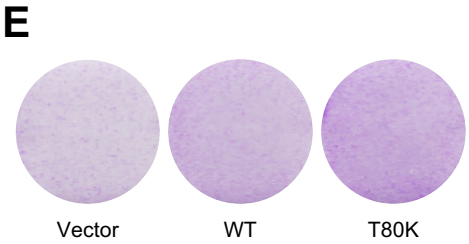
E
Vector
WT
T80K

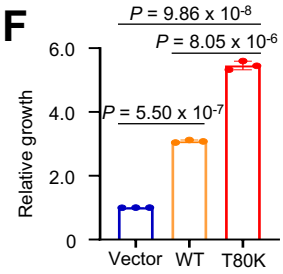
F
P = 9.86 x 10-8
P = 8.05 x 10-6
P = 5.50 x 10-7
Relative growth
Vector
WT
T80K

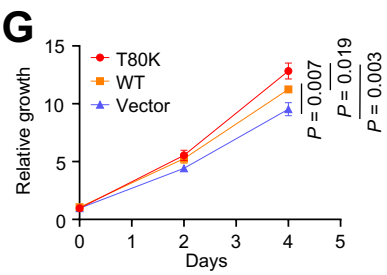
G
T80K
WT
Vector
P = 0.007
P = 0.019
P = 0.003
Relative growth
Days

Figure 7

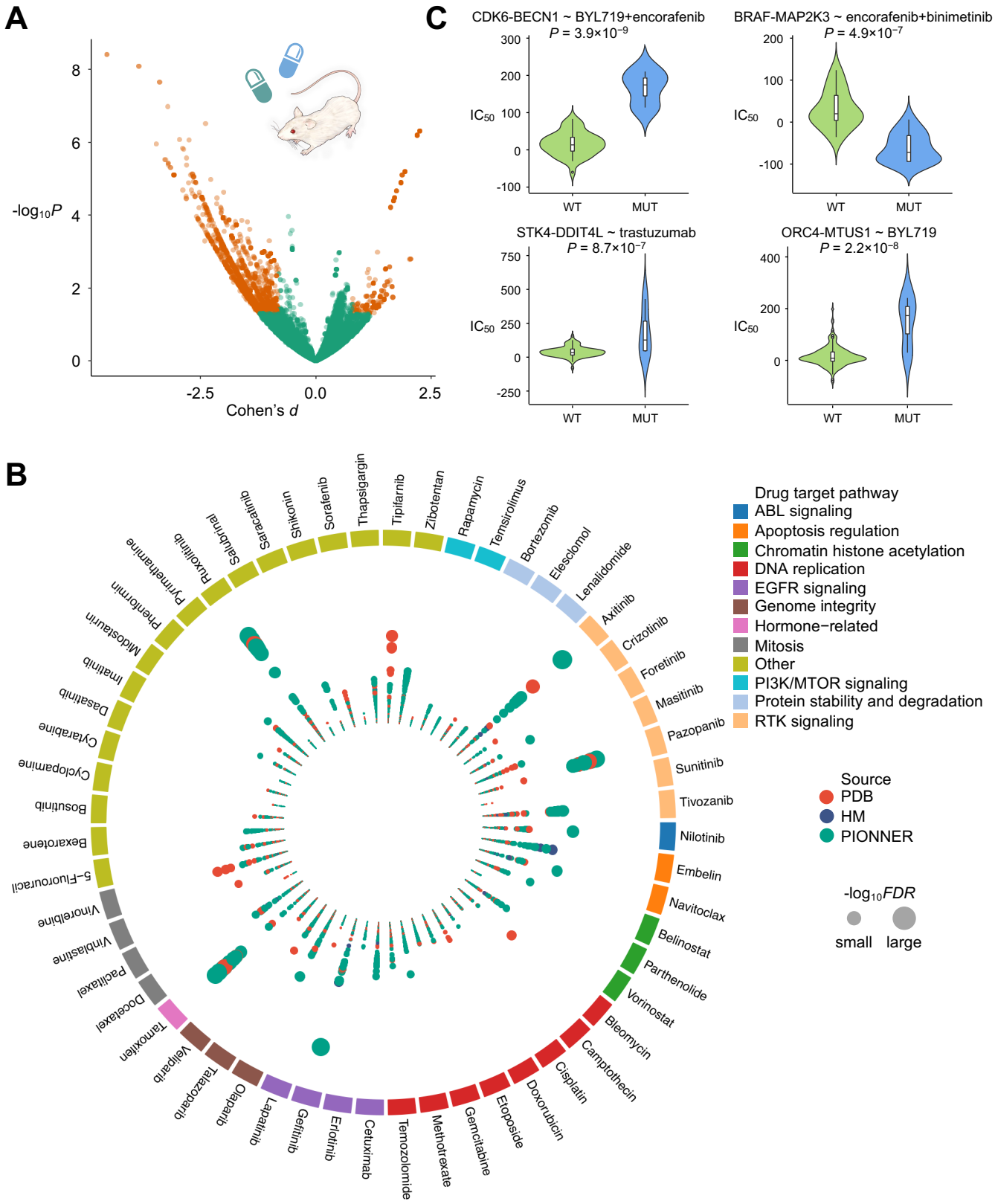
A
-log10P
Cohen's d
C
CDK6-BECN1 ~ BYL719+encorafenib
P = 3.9×10−9
BRAF-MAP2K3 ~ encorafenib+binimetinib
P = 4.9×10−7
STK4-DDIT4L ~ trastuzumab
P = 8.7×10−7
ORC4-MTUS1 ~ BYL719
P = 2.2×10−8
IC50
WT
MUT
B
Drug target pathway
ABL signaling
Apoptosis regulation
Chromatin histone acetylation
DNA replication
EGFR signaling
Genome integrity
Hormone−related
Mitosis
Other
PI3K/MTOR signaling
Protein stability and degradation
RTK signaling
Source
PDB
HM
PIONNER
-log10FDR
small
large
Thapsigargin
Tipifarnib
Zibotentan
Rapamycin
Temsirolimus
Bortezomib
Elesclomol
Lenalidomide
Axitinib
Crizotinib
Foretinib
Masitinib
Pazopanib
Sunitinib
Tivozanib
Nilotinib
Embelin
Navitoclax
Belinostat
Parthenolide
Vorinostat
Bleomycin
Camptothecin
Cisplatin
Doxorubicin
Etoposide
Gemcitabine
Methotrexate
Temozolomide
Cetuximab
Erlotinib
Gefitinib
Lapatinib
Olaparib
Talazoparib
Veliparib
Tamoxifen
Docetaxel
Paclitaxel
Vinblastine
Vinorelbine
5-Fluorouracil
Bexarotene
Bosutinib
Cyclopamine
Cytarabine
Dasatinib
Imatinib
Mitoxantrone
Pirfenidone
Pyrimethamine
Ruxolitinib
Salubrinal
Saracatinib
Shikonin
Sorafenib

Figure 8

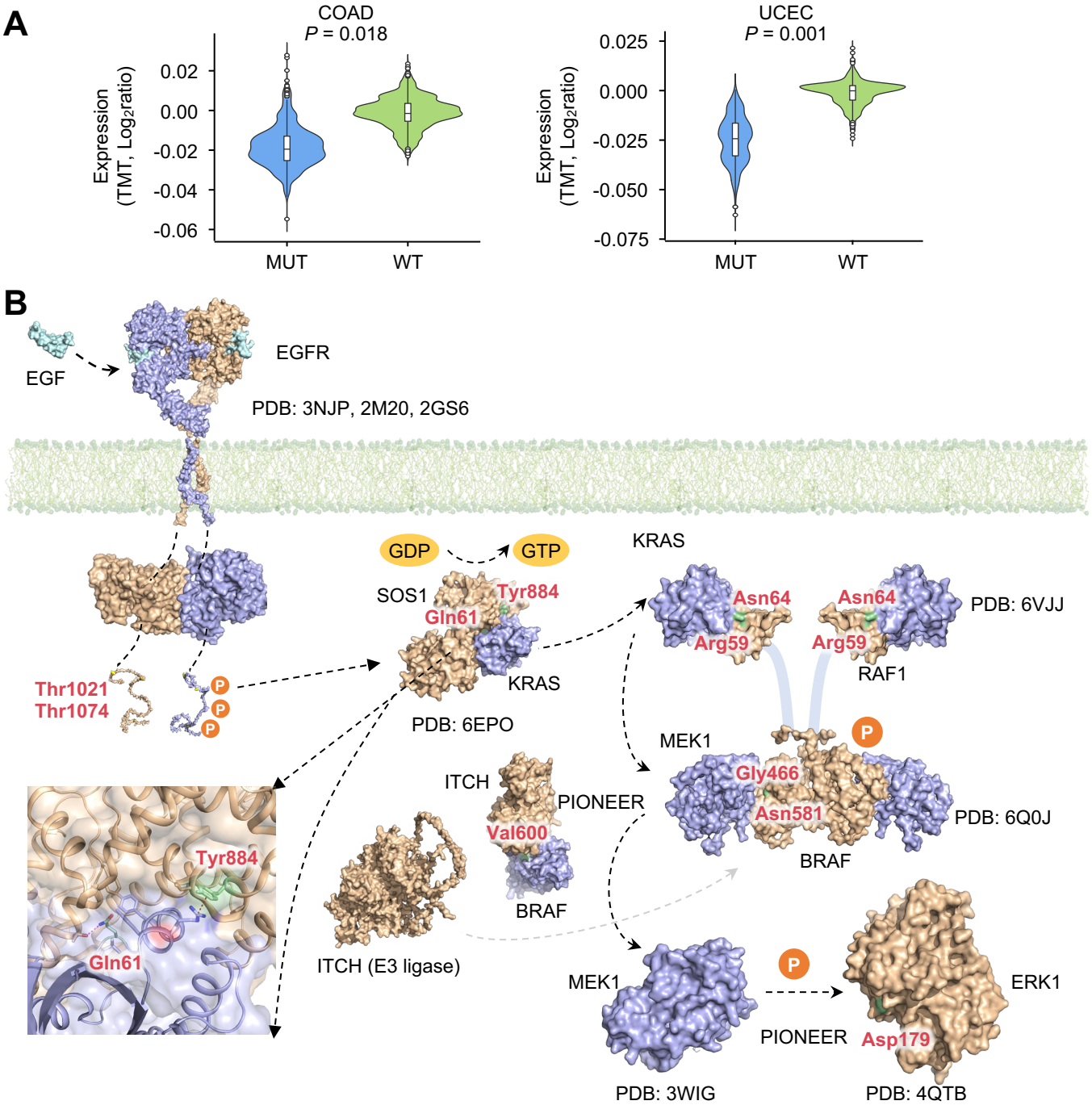
A
COAD
P = 0.018
Expression (TMT, Log2ratio)
0.02
0.00
-0.02
-0.04
-0.06
MUT
WT
UCEC
P = 0.001
0.025
0.000
-0.025
-0.050
-0.075
B
EGF
EGFR
PDB: 3NJP, 2M20, 2GS6
GDP
GTP
SOS1
Tyr884
Gln61
KRAS
PDB: 6EPO
Thr1021
Thr1074
P
KRAS
Asn64
Arg59
PDB: 6VJJ
RAF1
MEK1
Gly466
Asn581
BRAF
PDB: 6Q0J
ITCH
PIONEER
Val600
BRAF
ITCH (E3 ligase)
Tyr884
Gln61
MEK1
PIONEER
ERK1
Asp179
PDB: 3WIG
PDB: 4QTB

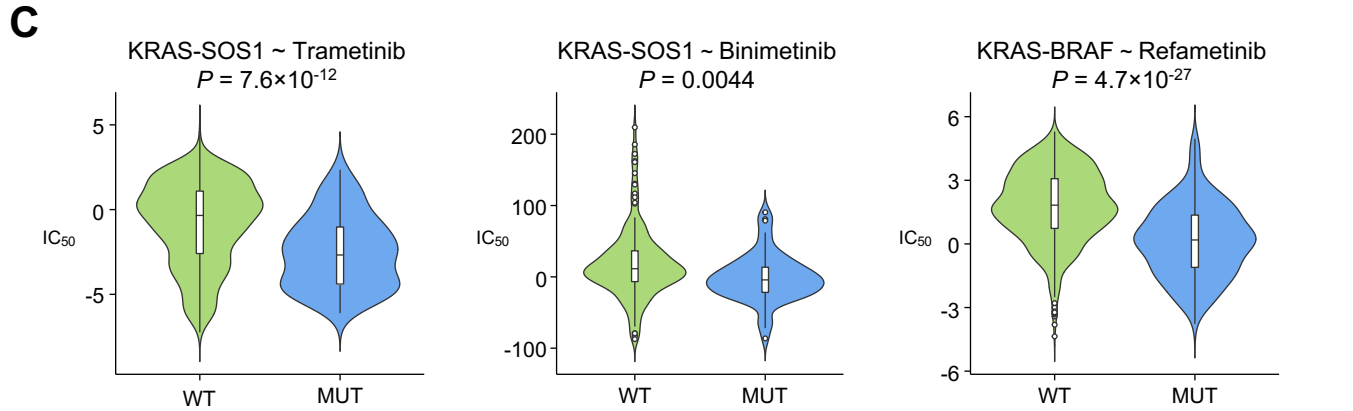
C
KRAS-SOS1 ~ Trametinib
P = 7.6×10-12
KRAS-SOS1 ~ Binimetinib
P = 0.0044
KRAS-BRAF ~ Refametinib
P = 4.7×10-27
IC50
WT
MUT